

Subaru IR Echelle Spectroscopy of Herbig-Haro Driving Sources

I. H₂ and [Fe II] Emission¹

M. Takami^{1,2}, A. Chrysostomou², T.P. Ray³, C.J. Davis⁴, W.R.F. Dent⁵, J. Bailey⁶, M. Tamura⁷, H. Terada¹, T.S. Pyo¹

mtakami@subaru.naoj.org

ABSTRACT

We present infrared echelle spectroscopy of three Herbig-Haro (HH) driving sources (SVS 13, B5-IRS 1 and HH 34 IRS) using Subaru-IRCS. The large diameter of the telescope and wide spectral coverage of the spectrograph allowed us to detect several H₂ and [Fe II] lines in the *H*- and *K*-bands. These include H₂ lines arising from $v=1-3$ and $J=1-11$, and [Fe II] lines with upper level energies of $E/k = 1.1 - 2.7 \times 10^4$ K. For all objects the outflow is found to have two velocity components: (1) a high-velocity (-70 to -130 km s⁻¹) component (HVC), seen in [Fe II] or H₂ emission and associated with a collimated jet; and (2) a low-velocity (-10 to -30 km s⁻¹) component (LVC), which is seen in H₂ emission only and is spatially more compact. Such a kinematic structure resembles optical forbidden emission line outflows associated with classical T Tauri stars, whereas the presence of H₂ emission reflects the low-excitation nature of the outflowing gas close to these protostars. The observed H₂ flux ratios indicate a temperature of $2 - 3 \times 10^3$ K, and a gas density of 10^5 cm⁻³ or more, supporting shocks as the heating mechanism. B5-IRS 1 exhibits faint extended emission associated with the H₂-LVC, in which the radial velocity slowly increases with distance from the

¹Subaru Telescope, 650 North A'ohoku Place, Hilo, Hawaii 96720, USA

²Centre for Astrophysics Research, University of Hertfordshire, Hatfield, HERTS AL10 9AB, UK

³School of Cosmic Physics, Dublin Institute for Advanced Studies, 5 Merrion Square, Dublin 2, Ireland

⁴Joint Astronomy Centre, 660 North A'ohoku Place, University Park, Hilo, Hawaii 96720, USA

⁵UK Astronomy Technology Centre, Royal Observatory, Blackford Hill, Edinburgh EH9 3HJ, UK

⁶Australian Centre for Astrobiology, Macquarie University, NSW 2109, Australia

⁷National Astronomical Observatory of Japan, Osawa, Mitaka, Tokyo 181-8588, Japan

protostar (by $\sim 20 \text{ km s}^{-1}$ at $\sim 500 \text{ AU}$). This is explained as warm molecular gas entrained by an unseen wide-angled wind. The [Fe II] flux ratios indicate electron densities to be $\sim 10^4 \text{ cm}^{-3}$ or greater, similar to forbidden line outflows associated with classical T Tauri stars. Finally the kinematic structure of the [Fe II] emission associated with the base of the B5-IRS 1 and HH 34 IRS outflows is shown to support disk-wind models.

Subject headings: stars: formation — ISM: jets and outflows — ISM: kinematics and dynamics — line: formation

1. Introduction

Mass accretion and ejection are fundamental processes for the evolution of young stellar objects (YSOs). Understanding their mechanisms, and also physical conditions which determine stellar masses, is one of the major challenges of contemporary astrophysics. Mass accretion cannot proceed without removing angular momentum from the surrounding material. Theories predict that outflowing gas plays an important role in this process (see e.g. Blandford & Payne 1982; Shu et al. 2000; Königl & Pudritz 2000). However, there are two crucial problems which hinder the investigation of this scenario through observations. One is the limited spatial resolution of telescopes, which has not been sufficient to fully resolve the jet/wind launching region, i.e. where the angular momentum transfer may occur. The other is the fact that such a region is often deeply embedded within a massive envelope, making it difficult to observe at optical to near-IR wavelengths.

Even so, classical T-Tauri stars, a class of low-mass YSOs, are directly observable at optical-UV wavelengths, allowing the study of mass accretion and ejection to within 100 AU of the central star for nearby sources. Studies of UV excess continuum and permitted emission lines strongly suggest that stellar bipolar magnetic fields are coupled to the inner edge of the disk at a few stellar radii, regulating stellar rotation to well below the break-up velocity (see, e.g., Calvet et al. 2000 and Najita et al. 2000 for reviews). Disk material seems to lose a significant amount of angular momentum at the inner edge of the disk, before falling down magnetic field lines and being shocked near the stellar surface. Such “magnetospheric accretion flow” is indeed observed as redshifted absorption in permitted lines (see, e.g., Najita et al. 2000). At the same time, a jet and/or wind seems to be launched within a few AU of the

¹Based on data collected at the Subaru Telescope, which is operated by National Astronomical Observatory of Japan

disk or at the inner disk edge. A physical link between these two phenomena is indicated by the fact that disk accretion rates, measured from the veiling continuum, are correlated with mass outflow signatures such as forbidden line luminosities (Hartigan, Edwards, & Ghandour 1995; Calvet 1997). Using the *Hubble Space Telescope (HST)* Bacciotti et al. (2002), Coffey et al. (2004) and Woitas et al. (2005) show that the internal motion of forbidden line outflows is consistent with flow rotation. These results agree with the scenario that the flow removes angular momentum from the disk, thereby allowing mass accretion to occur. Studying the kinematics of outflowing gas at AU scales, which cannot be directly resolved by the *HST* or adaptive optics with 8-10 m telescopes, could provide more crucial information for understanding their ejection. This spatial scale is being explored using the technique of spectro-astrometry which allows the spatial structure of emission/absorption features to be studied down to milliarcsecond scales (e.g., Bailey 1998; Takami et al. 2001; Takami, Bailey & Chrysostomou 2003; Whelan et al. 2004).

However, there is growing evidence that the stellar mass has almost been determined at younger evolutionary phases (Class 0–I phases), and mass accretion at the T Tauri phase is responsible for only a tiny fraction of the entire stellar mass (of order 1% — see Calvet et al. 2000). It is often assumed, but not confirmed, that disk accretion within 100 AU of Class I protostars occurs by the same mechanism as for T Tauri stars. Br γ line profiles observed towards Class I protostars suggest that these stars are associated with magnetospheric accretion columns like T Tauri stars (see e.g., Davis et al. 2001). However, measured Br γ luminosities suggest that steady magnetospheric mass accretion can explain only a few percent of the total stellar mass, requiring episodic and violent mass accretion (see Calvet et al. 2000).

Class 0–I protostars also exhibit signatures of energetic mass ejection as optical jets and molecular bipolar outflows (see e.g., Reipurth & Bally 2001 and Richer et al. 2000 for reviews). While the extended parts of these outflows have been observed over decades, kinematics of outflowing gas within a few hundred AU has just begun to be revealed by near-IR high-resolution spectroscopy and spectro-imaging. Davis et al. (2001) observed H₂ 2.122 μ m emission at several HH driving sources, showing the presence of Molecular Hydrogen Emission Line (MHEL) regions, analogous to the forbidden emission line (FEL) regions associated with T Tauri stars. The H₂ emission shows a variety of profiles with multiple velocity peaks similar to FELs in T-Tauri stars. The kinematics of the H₂ 2.122 μ m emission differs from that of the [Fe II] 1.644 μ m emission, revealing complicated kinematic structure (Davis et al. 2003). At the same time Fabry-Perot observations (Davis et al. 2002) show the presence of small scale jets traced by H₂ emission, analogous to forbidden line jets associated with classical T Tauri stars. Evidence for H₂ emission from cavity walls is also seen for a few objects, suggesting the presence of a wide-angled wind.

Detailed studies of mass ejection in these objects could lead us to understand the mechanism of mass accretion, which is responsible for determining the stellar mass. We thus performed an extensive study of MHEL regions and [Fe II] emission line regions associated with three HH driving sources using Subaru-IRCS.

The rest of the paper is organised as follows. In §2 we describe the observations and data reduction methods. In §3 we present the observed kinematics seen in the H₂ 2.122 μm and [Fe II] 1.644 μm emission, the brightest H₂ and [Fe II] emission in our spectra. In §4 we derive the extinction, density and temperature inferred from H₂ and [Fe II] line ratios. In §5 we compare our results with forbidden line outflows associated with T Tauri stars, and investigate the mechanism of driving jets/winds for low-mass YSOs. In Paper II we show the results for other emission lines including CO and atomic lines.

2. Observations

Observations were made on 2002 November 25 at the SUBARU 8.2-m telescope using the Infrared Camera and Spectrograph IRCS (Tokunaga et al. 1998; Kobayashi et al. 2000). The echelle grating mode with a 0.3'' wide slit provides a spectral resolution of 1.1×10^4 , corresponding to a velocity resolution of 28 km s^{-1} . The pixel scale of 0.06'' provides better than Nyquist sampling of the seeing ($\sim 0.6''$), thereby allowing us to investigate spatial structures on sub-arcsecond scales.

Table 1 shows the log of the observations. Three targets, SVS 13, B5-IRS 1 and HH 34 IRS, were selected from Davis et al. (2001, 2003) based on the strength of the H₂ and [Fe II] emission in their proximity. Details of the individual targets are described in Appendix A. Spectra in *H*- and *K*-bands were obtained along the jet axis for all objects, and *K*-band spectra perpendicular to the jet axis were also obtained for SVS 13. These cross-dispersed spectra in *H*- and *K*-bands cover 1.52–1.78 μm (orders 37–32) and 1.96–2.45 μm (orders 28–23), respectively. Thus they include a number of [Fe II] and H₂ lines, thereby allowing for accurate measurements of their relative fluxes. At each slit position, object-sky-object sequences were repeated each with an exposure time of 120–180 seconds. Spectra at opposite slit angles ($\Delta\text{P.A.} = 180^\circ$) were also obtained to remove bad pixels. In addition to the targets, A-type bright standards were observed at similar airmasses to correct for telluric absorption. The flat fields were made by combining many exposures of the spectrograph illuminated by a halogen lamp.

The data were reduced using the FIGARO and KAPPA packages². The position-velocity diagrams were obtained via standard reduction processes: i.e., dark-subtraction, flat-fielding, removal of bad pixels, night sky subtraction, correcting for curvature in the echelle spectra, wavelength calibration and correcting for telluric absorption. Wavelength calibrations were made using OH airglow and telluric absorption lines giving an uncertainty in the calibration of less than $\pm 4 \text{ km s}^{-1}$. Before correcting for telluric absorption, Brackett-series absorption features were removed from the spectra of the standard stars by Lorentzian fitting.

The sky was not photometric, thus the relative flux between H - and K -band spectra had to be carefully calibrated. We did this by scaling one of the two spectra for each target so that a fit to the continuum in the two bands could be made using a single linear or polynomial function. For SVS 13, we were not able to fit the entire continuum with a single linear/polynomial function due to the presence of H_2O emission bands (see Carr, Tokunaga, & Najita 2004). The fitting was thus carried out only for limited spectral ranges near the boundary of the H - and K -bands ($1.63\text{--}1.78/1.96\text{--}2.05 \mu\text{m}$). For B5-IRS 1 and HH 34 IRS, the entire continuum was used for the fitting. The results are shown in Figure 1. Fitting errors suggest uncertainties for the relative fluxes between H - and K -band spectra to be 2, 4 and 6 % for SVS 13, B5-IRS 1 and HH 34 IRS, respectively. The $2.25/1.65 \mu\text{m}$ continuum flux ratio measured in SVS 13 is 1.58, in excellent agreement with that in the $0.8\text{--}2.5 \mu\text{m}$ spectrum obtained by Carr et al. (2004).

3. H_2 1–0 S(1) and [Fe II] 1.644 μm Emission

Figure 2 shows the position-velocity (P-V) diagrams of the H_2 2.122 μm and [Fe II] 1.644 μm emission, the brightest H_2 and [Fe II] lines. To show the kinematic and intensity distribution in detail, we extract line profiles at different positions and velocities and plot them in Figure 3. All velocities quoted are in the local standard of rest (LSR) frame. In the following subsections we describe the results for individual objects.

3.1. SVS 13

Echelle spectroscopy by Davis et al. (2001, 2003) revealed the following kinematic components in H_2 and [Fe II] emission: (1) two velocity components in the H_2 emission peaking at -90 and -20 km s^{-1} ; and (2) two velocity components in the [Fe II] emission

²see <http://star-www.rl.ac.uk/>

at -130 km s^{-1} and -20 to -50 km s^{-1} . The authors measured typical spatial offsets for the H_2 emission of $0.4''$ and $0.2''$ from the star for the high- and low-velocity components, respectively. Fabry-Perot imaging shows that the H_2 emission at SVS 13 is associated with a collimated small-scale jet (Davis et al. 2002).

Our results confirm the presence of three out of the four velocity components identified by Davis et al. (2001, 2003). These are: the two velocity components in H_2 and the high velocity component in $[\text{Fe II}]$. In Figures 2 and 3 the high-velocity component (HVC) of H_2 emission is extended over a few arcsec, peaking at $1.3''$ with a FWHM velocity of $\sim 70 \text{ km s}^{-1}$. This component coincides with the small-scale H_2 jet seen in Fabry-Perot images by Davis et al. (2002). The centroid velocity of the H_2 HVC coincides with the high velocity peak of HH 7–10, the extended blueshifted outflow associated with SVS 13, observed in atomic and H_2 lines (Solf & Böhm 1987; Hartigan et al. 1987; Movsessian et al. 2000; Davis et al. 2000, 2001). We thus conclude that this HVC component for H_2 is the base of the extended HH outflow.

The low velocity component (LVC) of the H_2 emission is only marginally resolved, both spatially and spectroscopically. This indicates that its spatial scale and velocity dispersion are comparable to the seeing ($0.6''$) and spectral resolution (28 km s^{-1}), respectively. The centroidal position of the H_2 LVC is offset from the star by $0.2''$ – $0.3''$, consistent with previous spectro-astrometric measurements (Davis et al. 2001). Figure 3 shows that the H_2 emission across the jet axis marginally extends to the north-east.

$[\text{Fe II}]$ emission is spatially unresolved, with a centroid position of $\sim 0.1''$ offset from the continuum towards the jet. The line exhibits a FWHM velocity of 36 – 38 km s^{-1} , slightly larger than the spectral resolution of 28 km s^{-1} . Interestingly, its centroid position decreases as the velocity increases: $0.15''$ at -105 km s^{-1} to $0.05''$ at -150 km s^{-1} . This tendency contrasts with that normally found for forbidden line emission in T Tauri stars, in which the centroid position increases with velocity (see e.g., Takami et al. 2001; Whelan et al. 2004).

3.2. B5-IRS 1

High-resolution spectroscopy by Yu, Billawala, & Bally (1999) and Davis et al. (2001) measured an LSR velocity for the H_2 $2.122 \mu\text{m}$ emission of -10 to 4 km s^{-1} , i.e., 6 – 20 km s^{-1} blueshifted from the systemic velocity of the parent cloud. The H_2 emission did not show any spatial extension at the driving source, while the presence of H_2 emission at HH 366 E5 was seen $20''$ away. Echelle spectroscopy by Davis et al. (2003) revealed two components of $[\text{Fe II}]$ emission associated with the driving source, peaking at -140 and -70 km s^{-1} . The

high velocity emission at -140 km s^{-1} was found to be extended towards the jet.

The H_2 emission in Figures 2 and 3 show two components at similar low velocities – a bright component peaking at $0.2''$ – $0.3''$ from the star, and a faint component extending towards the jet over a few arcsec. The bright component shows a centroidal LSR velocity of -2 km s^{-1} , about $\sim 10 \text{ km s}^{-1}$ blueshifted from the systemic velocity of the parent molecular cloud. This component is only marginally resolved both spatially and spectroscopically (with seeing at $0.6''$ and spectral resolution of 28 km s^{-1}). The centroid velocity of the H_2 emission increases with distance: -7 and -20 km s^{-1} at $1''$ and $2''$ from the star, respectively.

Similarly, the [Fe II] emission also consists of two components: a bright component within an arcsec of the star and an extended component towards HH 366E. The bright component is not spatially resolved, and offset $0.4''$ towards the jet. This component shows a wide velocity range (0 to -200 km s^{-1}) with the position gradually increasing with velocity. Figure 2 shows three peaks for this component, appearing at positions: (-75 km s^{-1} , $0.2''$), (-115 km s^{-1} , $0.1''$), and (-160 km s^{-1} , $0.4''$). The faint extended component is at a velocity of $\sim -140 \text{ km s}^{-1}$, and is not spectroscopically resolved. The velocity differs remarkably from HH 366E ($\sim -20 \text{ km s}^{-1}$ — Bally, Devine, & Alten 1996), however, its low velocity dispersion relative to the centroid velocity suggests that the emission is associated with a collimated jet (see Eislöffel et al. 2000a).

3.3. HH 34 IRS

Echelle spectroscopy by Davis et al. (2001) showed that H_2 emission at HH 34 IR has a velocity of 1 km s^{-1} , which is $\sim 10 \text{ km s}^{-1}$ blueshifted from the systemic velocity of the parent cloud. Davis et al. (2003) showed that [Fe II] emission at the driving source peaks at $-95 (\pm 10) \text{ km s}^{-1}$. The line profile they observed shows an extended wing towards the systemic velocity of the parent cloud.

In our spectra, the H_2 emission shows a LSR velocity range of -20 to 20 km s^{-1} . It is not spectroscopically resolved, indicating that the velocity dispersion is smaller than 28 km s^{-1} . The peak H_2 emission is spatially offset by $\sim 0.1''$ and shows faint extension toward the jet up to $1''$ from the star. The HVC is not seen in H_2 towards HH 34, in contrast to SVS 13 and analogous to B5-IRS 1.

The [Fe II] emission in Figures 2 and 3 shows a broad component near the base of the jet while the jet itself is narrower in the diagram. Such a result is consistent with previous echelle spectroscopy by Davis et al. (2003). In contrast to B5-IRS 1, these two components are similarly bright. The former shows a single peak at the velocity of the jet (-90 to

-100 km s^{-1} — Davis et al. 2003), while the latter shows three peaks at $(-90 \text{ km s}^{-1}, 0.1'')$, $(-100 \text{ km s}^{-1}, 0.9'')$, and $(-90 \text{ km s}^{-1}, 1.5'')$. These positions coincide with the knots in the jet seen in *HST* images, which peak at $0.0''$ (A6), $0.5''$ (A5), and $1.2''$ (A4) from the driving source (Reipurth et al. 2002). Slight differences in positions between these two observations are attributed to their proper motions, which are $0.11/0.13/0.02 \text{ arcsec/yr}$ for A4/A5/A6, respectively (Reipurth et al. 2002).

4. H₂ and [Fe II] Lines and Inferred Extinction, Temperature and Density

The spectra presented here contain a number of H₂ and [Fe II] lines in addition to the bright H₂ 1–0 S(1) $2.122 \mu\text{m}$ and [Fe II] $1.644 \mu\text{m}$ lines. These include H₂ emission arising from $v = 1 - 3$ and $J = 1 - 11$, and [Fe II] emission with upper state energies $E/k = 1 - 3 \times 10^4 \text{ K}$. It is noteworthy that we detect a few [Fe II] $^2P \rightarrow ^4P$ lines in the *K*-band, which is presumably their first detection in YSOs. Figures 4 and 5 show PV diagrams of bright H₂ and [Fe II] lines, respectively. Although the signal-to-noise ratios of some lines are not high enough to investigate their kinematic structure, the H₂ lines appear similar to those of H₂ 1–0 S(1). Regarding [Fe II] emission, the $^4D \rightarrow ^4F$ lines all show similar kinematic structure, while $^2P \rightarrow ^4P$ lines appear spatially compact at the driving source.

The relative line fluxes in the regions shown in Figures 4 and 5 were measured and tabulated in Tables 2 and 3. These regions are labeled as Regions 1 to N ($N=1-5$) for each object and line (H₂/[Fe II]). The measured flux ratios are used in the following sections to investigate the physical conditions of, and extinction, to the H₂ and [Fe II] emission line regions.

4.1. Extinction

If two emission lines share the same upper energy level, their flux ratio depends only on the extinction and physical constants. The measured flux ratio of these lines can thus be used to determine the extinction towards the emission line regions. Such pairs in our spectra include: H₂ 1–0 S(1) $2.122 \mu\text{m}$ and 1–0 Q(3) $2.424 \mu\text{m}$; 1–0 S(0) $2.223 \mu\text{m}$ and 1–0 Q(2) $2.413 \mu\text{m}$; 1–0 S(2) $2.034 \mu\text{m}$ and 1–0 Q(4) $2.437 \mu\text{m}$; [Fe II] $a^4D_{3/2} \rightarrow a^4F_{7/2}$ $1.600 \mu\text{m}$ and $a^4D_{3/2} \rightarrow a^4F_{5/2}$ $1.712 \mu\text{m}$; $a^4D_{1/2} \rightarrow a^4F_{5/2}$ $1.664 \mu\text{m}$ and $a^4D_{1/2} \rightarrow a^4F_{3/2}$ $1.745 \mu\text{m}$. Tables 4 and 5 show extinction obtained using these lines, adopting transition probabilities for H₂ and Fe⁺ by Turner, Kirby-Docken & Dalgarno (1977) and Nussbaumer & Storey (1988), respectively. For an extinction law we adopt $A_\lambda = A_V \times \lambda^{-1.6}$, based

on $A_H/A_V = 0.175$ and $A_K/A_V = 0.112$ obtained for diffuse interstellar clouds (Rieke & Lebofsky 1985).

Different pairs of emission lines result in markedly different values for the extinction. For instance, in H₂ Region 1 of SVS 13, the extinction measured from all three ratios significantly differ, A_V ranging from <1 to ~ 15 . In contrast, values derived from the S(0)/Q(2) and S(1)/Q(3) ratios are the same as each other in Region 1 of B5 IRS 1 within an uncertainty of 20%. Concerning [Fe II] emission, extinction obtained from the 1.712/1.600 μm ratio is systematically lower than those obtained from the 1.745/1.664 μm ratio. The discrepancies in A_V are greater than a factor of two in some cases. This might be interpreted as the assumed power law ($A_V \times \lambda^{-1.6}$) being invalid. However, a power law index of -1 or -2 instead of -1.6 changes the discrepancies by only 2–3 %, due to a similarity of wavelengths between line pairs. Therefore, this cannot explain the discrepancies in A_V described above.

Systematic discrepancies of extinction obtained from [Fe II] 1.712/1.600 μm and 1.745/1.664 μm ratios may be due to errors in adopted transition probabilities. Possible errors for [Fe II] transitions are also reported by Bautista & Pradhan (1998), who studied optical [Fe II] spectra in the Orion Nebula. Regarding H₂ emission, Q-branch lines are in poorly transmitting atmospheric windows, and calibration errors by telluric absorption may also contribute to the apparently different extinctions described above.

Such uncertainties in the extinction will affect the determination of gas temperatures and densities in the following subsections. For the H₂ emission line regions we adopt the extinction obtained from the S(1)/Q(3) ratio for the following reasons: (1) consistency, as this ratio is often used in the literature (e.g., Gredel 1994; Eislöffel, Smith, & Davis 2000b); (2) when this ratio is obtained at the highest S/N ratio agrees with those measurements using the S(0)/Q(2) and/or S(2)/Q(4) ratios; and (3) both S(1) and Q(3) lines are in relatively clean parts of the atmospheric window. For [Fe II] emission we regard any extinction obtained from the 1.712/1.600 μm ratio as upper limits.

4.2. Excitation, Temperature and Density in H₂ Emission Line Regions

Figure 6 shows a population diagram of ro-vibrationally excited H₂ obtained from our spectra. The figure shows that molecular hydrogen in all regions is thermally excited at a temperature of $2 - 3 \times 10^3$ K. In particular, the temperature obtained from the 2–1 S(1)/1–0 S(1) flux ratio is consistently stable at 2×10^3 K for all regions and objects. These trends are often observed in shocks associated with extended outflows (e.g., Burton et al. 1989; Gredel 1994; Eislöffel et al. 2000b). Thermal excitation of infrared H₂ emission could

also be attained via UV/X-ray heating (e.g., Burton, Hollenbach & Tielens 1990; Maloney, Hollenbach, & Tielens 1996; Tine et al. 1997) or ambipolar diffusion (Safier 1993). However, these models predict that line flux ratios strongly depend on the radiation field and gas density, or distance from the driving source. We thus conclude that shock excitation is a robust mechanism for the H₂ emission.

We can fit the level populations in Figure 6 using a single temperature line or curve for most of the regions and objects. In contrast, in Region 3 of SVS 13, the vibrational temperature at $v = 1$ and $J = 0 - 3$ shows a temperature of 2×10^3 K, lower than the rotational temperature at $v = 1$ (3×10^3 K). This indicates that the gas in this region has not attained LTE. Performing comparisons with population diagrams modelled by Gianninni et al. (2002), we estimate a H₂ number density of $\sim 10^7$ cm⁻³ for Region 3 of SVS 13, and $\sim 10^8$ cm⁻³ or greater for the other regions, assuming that thermal excitation is dominated by H₂-H₂ collisions. Collisional rate coefficients for H-H₂ collisions are ~ 100 times larger than H₂-H₂ collision for temperatures of $2 - 3 \times 10^3$ K (see e.g., Burton et al. 1990) thus the same results are also explained by hydrogen atomic number densities of $\sim 10^5$ cm⁻³ for Region 3 of SVS 13, and $\sim 10^6$ cm⁻³ or greater for the other regions. In either case, our results for SVS 13 suggest that the gas density decreases as one moves downstream of the shock: i.e., Region 2 to Region 3. This trend is also observed in HH outflows (e.g., Bacciotti & Eisöffel et al. 1999) and also so-called “micro-jets” in T Tauri stars (e.g., Lavalley-Fouquet, Cabrit, & Dougados 2000; Bacciotti et al. 2000; Woitas et al. 2002; Dougados, Cabrit, & Lavalley-Fouquet 2002).

H₂ population diagrams also allow us to discriminate between types of shock, e.g. C- and J-type shocks. Models predict that for energy levels $E/k = 0.5 - 2 \times 10^4$ K the level populations indicate a rather constant temperature for planar C-shocks while higher temperatures are required to excite the higher energy levels in planar J-shocks (see Eislöffel et al. 2000b, and references therein). To investigate this in detail, we show in Figure 6 the J-shock model prediction which empirically explains the H₂ populations observed in Orion KL (Brand et al. 1988) and supernova remnant IC 443 (Richter et al. 1995). The figure shows that the population in Region 3 of SVS 13 cannot be attributed to either a planar J-shock or an LTE model with a single temperature, representative of a planar C-shock. J/C-shock models with non-LTE populations and/or more complex geometries may be required to interpret the observations. For the other regions and objects, LTE seems to have been attained, although higher S/N data are required to discriminate between C- and J-shocks.

Fernandes & Brand (1995) observed a number of near-IR H₂ emission in HH 7, and argue the presence of UV-pumped H₂ emission based on their results. Although this excitation mechanism can provide non-LTE H₂ populations, it cannot explain the non-LTE population

observed in Region 3 of SVS 13. In Figure 6, the population at $v=1$ and $J=1-11$ indicates a rotational temperature of $\sim 3 \times 10^3$ K in this region, while that at $v=1-2$ and low- J levels indicates a vibrational temperature of $\sim 2 \times 10^3$ K, lower than the other. This trend is opposite as observed in UV-pumped H_2 regions, in which rotational temperatures are lower than vibrational temperatures (see e.g., Hasegawa et al.; Tanaka et al. 1989).

4.3. Electron Density and Temperature in [Fe II] Emission Line Regions

To investigate electron densities and temperatures of the [Fe II] emission line regions, we have developed a non-LTE model which considers the first 16 fine structure levels. Transition probabilities are taken from Nussbaumer & Storey (1988), the energy levels are from the NIST Atomic Spectra Database³, and the rate coefficients for electron collisions are from Zhang & Pradhan (1995). All radiative transitions among these levels are quadrupole or magnetic dipole type, thus we assume optically thin conditions and compute level populations under statistical equilibrium. This model is essentially the same as that developed by Zhang & Pradhan (1995), Nisini et al. (2002) and Pesenti et al. (2003), although we provide the following two new line flux ratios: $I_{1.664 \mu m} / I_{1.644 \mu m}$, which is not sensitive to extinction, and, $I_{1.749 \mu m} / I_{1.644 \mu m}$, which is highly sensitive to the electron temperature as well as the electron density.

Figure 7 shows the modelled and observed line flux ratios. For SVS 13 we assume either no extinction ($A_V = 0$) or $A_V = 20$, obtained using the $I_{1.257 \mu m} / I_{1.644 \mu m}$ ratio by Gredel (1996). The $I_{1.533 \mu m} / I_{1.644 \mu m}$ ratio is the least sensitive to the electron temperature, and these two lines are brighter than the other ${}^4D \rightarrow {}^4F$ transitions such as the 1.600 and 1.664 μm lines (see Table 3). This ratio is thus often used to derive an electron density (see e.g., Hamann et al. 1994; Itoh et al. 2000; Pesenti et al. 2003). However, Figure 7 shows that a combination of $I_{1.600 \mu m} / I_{1.644 \mu m}$ and $I_{1.664 \mu m} / I_{1.644 \mu m}$ ratios provide electron densities with better accuracies in some cases since these are not much affected by the uncertainty in extinction described in §4.1.

Figure 7 shows that the electron density of [Fe II] emission line regions $n_e \sim 10^4 \text{ cm}^{-3}$ or greater in all the objects and regions we observe. Such a density is similar to [Fe II] emission line regions associated with T Tauri stars (Hamann et al. 1994). In B5-IRS 1 and HH 34 IRS, $I_{1.664 \mu m} / I_{1.644 \mu m}$ and $I_{1.600 \mu m} / I_{1.644 \mu m}$ (and also the $I_{1.533 \mu m} / I_{1.644 \mu m}$ ratios in HH 34 IRS) are lower at the extended part than the base, indicating that the electron density decreases downstream of the jet. As previously stated such a trend is also observed

³<http://physics.nist.gov/cgi-bin/AtData/main.asd>

in previous observations of extended HH outflows (e.g., Bacciotti & Eisöffel et al. 1999) and also “micro-jets” in T Tauri stars (e.g., Lavalley-Fouquet et al. 2000; Bacciotti et al. 2000; Woitas et al. 2002; Dougados et al. 2002).

As shown in Figure 7, the $I_{1.533\mu\text{m}}/I_{1.644\mu\text{m}}$, $I_{1.600\mu\text{m}}/I_{1.644\mu\text{m}}$, $I_{1.664\mu\text{m}}/I_{1.644\mu\text{m}}$ ratios are not sensitive to electron temperature due to their upper energy levels being similar to each other. The lines with significantly different upper energy levels, such as ${}^4P \rightarrow {}^4D$ 1.749 μm , are required with better accuracy to determine the electron temperature. The temperature inferred by the $I_{1.749\mu\text{m}}/I_{1.644\mu\text{m}}$ ratio appears to be similar to that of forbidden emission line regions associated with T Tauri stars ($\sim 10^4$ K, e.g., Hamann 1994; Dougados et al. 2002) and extended HH objects ($\sim 10^4$ K, e.g., Bacciotti & Eisöffel 1999), although higher S/N ratios are required to determine this parameter.

4.4. [Fe II] ${}^2P \rightarrow {}^4P$ lines as a new probe for jets

Figure 8 shows the energy level diagram of Fe^+ highlighting the transitions detected in this work. In addition to transitions at the lowest 16 levels, which are often observed and modelled, our spectra exhibit several ${}^2P \rightarrow {}^4P$ lines between 2.007 and 2.244 μm . The upper level energies of these transitions are $\sim 2.6 \times 10^4$ K, more than twice as large as the 1.644 μm line (1.1×10^4 K). Due to longer wavelengths, these lines suffer from less extinction than the bright [Fe II] lines in the H -band: A_λ is 30–40 % smaller than for the 1.644 μm line.

Figure 9 shows the spatial distributions and line profiles of four [Fe II] emission lines, including two ${}^2P \rightarrow {}^4P$ lines at 2.047 and 2.133 μm . In HH 34 IRS that the 2.047 and 2.133 μm emission is concentrated at the base of the jet is in contrast to the 1.664 and 1.644 μm emission. At the driving source, the 2.047 and 2.133 μm emission have profiles similar to 1.644 μm emission. These trends are not clear in B5-IRS 1, although higher S/N ratios are required to investigate them in detail.

The compact spatial distribution, and also the line profiles, of the ${}^2P \rightarrow {}^4P$ lines at HH 34 IRS indicates that these lines could be powerful probes for studying the physical conditions of the flow accelerating region. HI recombination lines such as $\text{Br}\gamma$ have been used for over a decade as investigative tools of the jet/wind launching region (e.g., Natta, Giovanardi, & Palla 1988; Nisini, Antonucci, & Giannini 2004). However, the emission could originate from magnetospheric accretion columns even in Class I protostars as well as T Tauri stars (see e.g., Muzerolle et al. 1998; Davis et al. 2001). In contrast to this, but similar to the FEL regions in Class I protostars and T Tauri stars, the [Fe II] 2.047 and 2.133 μm lines

show only blueshifted components indicating that these are associated with outflowing gas. The absence of redshifted emission is attributed to obscuration of the counter flow by a disk or flattened envelope (see e.g., Appenzeller et al. 1984; Edwards et al. 1987).

Excitation conditions of the $^2P \rightarrow ^4P$ transitions are not clear due to large uncertainties in the collisional rate coefficients to the 2P level (see Zhang & Pradhan 1995; Verner et al. 1999). The spatial distribution observed at HH 34 IRS is either due to high temperature or density at the jet launching region. In addition, Verner et al. (2000) show that the level population of the 2P states is also affected by UV pumping, which could be efficient within an AU of YSOs. Accurate determination of collisional rate coefficients is desired to investigate the physical conditions of the jet/wind launching regions in detail.

5. Discussion

5.1. Comparison with T Tauri Stars — Flow Geometry and Heating

Jets/winds associated with T Tauri stars exhibit forbidden line emission seen within 10–100 AU of the star. The lines often exhibit two velocity components at high (-50 to -200 km s^{-1}) and low velocities (-5 to -20 km s^{-1} — see Eisloffel et al. 2000a for a review). High-resolution observations with the *Hubble Space Telescope* and ground-based adaptive optics have confirmed that the high-velocity component (hereafter HVC) is associated with a collimated jet (see e.g., Bacciotti et al. 2000; Woitas et al. 2002; Pyo et al. 2003). Emission line diagnostics to date suggest that this component is heated by shocks in internal working surfaces (see e.g., Lavalley-Fouquet et al. 2000; Takami et al. 2002; Dougados et al. 2002). In contrast to the HVC, the nature of the low velocity component (hereafter LVC) is still debated, although it appears to be associated with a compact ($< 50 \text{ AU}$) and wide-angled component of the flow (e.g., Bacciotti et al. 2000; Pyo et al. 2003). In addition to T Tauri stars, such a two-component kinematic structure to forbidden line emission is also observed at L1551-IRS 5, which is in transition from a Class I protostar to a T Tauri star (Pyo et al. 2002, 2005).

Davis et al. (2001) has shown that the H_2 $2.122 \mu\text{m}$ emission at HH driving sources has a similar kinematic structure to FEL regions in T Tauri stars. The similarities include: (1) both MHEL and FEL regions show blueshifted components at high (-50 to -150 km s^{-1}) and low (-5 to -20 km s^{-1}) velocities; (2) LVCs are more common than HVCs (see Hartigan et al. 1995 for FELs); (3) the HVC is spatially further offset from the exciting source than the LVC. Davis et al. (2003) showed that both H_2 and $[\text{Fe II}]$ $1.644 \mu\text{m}$ emission tend to be associated with each HH driving source. In their spectra the $[\text{Fe II}]$ is associated with higher

velocity gas than the H_2 , and peaks further away from the driving source in each system. This can be explained if the $[\text{Fe II}]$ is more closely associated with HH-type shocks in the inner, on-axis jet regions, while the H_2 is excited along the boundary between the jet and the near-stationary, dense ambient medium that envelopes the protostar.

As shown in §3, outflowing gas close to SVS 13, B5-IRS 1 and HH 34 IRS also show two blueshifted components i.e., a HVC associated with an extended collimated jet, and a LVC which is spatially more compact. In contrast to T Tauri stars, the LVC in all of these objects are observed in H_2 emission, and none of them show a low velocity peak in $[\text{Fe II}]$ emission. The observed line ratios indicate a temperature for the H_2 -LVC of $2 - 3 \times 10^3$ K, significantly lower than the LVC observed in T Tauri stars ($\sim 10^4$ K — Hamann 1994). The different temperatures arise from the fact that H_2 is dissociated at $T > 4000$ K, while a higher temperature is required to thermally excite Fe^+ and thus produce near-IR $[\text{Fe II}]$ emission.

In SVS 13, the HVC is observed in H_2 emission as well as the LVC. This contrasts to the HVC in B5-IRS 1 and HH 34 IRS, which are only observed in $[\text{Fe II}]$. The observed velocity of $\sim -70 \text{ km s}^{-1}$ in the H_2 HVC is nearly the same as for the forbidden line emission in the extended HH flow (Solf & Böhm 1987; Hartigan, Raymond, & Hartmann 1987; Movsessian et al. 2000). This suggests that H_2 is excited by shocks in the internal working surfaces, as observed in the HVC of T Tauri stars.

How does molecular hydrogen survive the jets/winds associated with Class I protostars? A few possible explanations come to mind. Bacciotti & Eisloffel (1999) have shown that the hydrogen ionization fraction generally decreases along the HH jet, suggesting the presence of a “prompt ionization” mechanism close to the source. Indeed, the presence of Alfvén wave heating or X-ray heating have been suggested at the base of outflows associated with classical T Tauri stars (e.g., Hartmann, Avrett, & Edwards 1982; Shang et al. 2002; Takami et al. 2003). Such ionization mechanisms could be less efficient in these Class I protostars due to, e.g., weaker chromospheric activity, thereby allowing molecular hydrogen to survive. Other explanations include: (1) the outflowing gas has a higher gas density, providing a high cooling efficiency behind the shocks; (2) magnetic cushioning occurs efficiently, leading to low levels of excitation and dissociation (e.g., Draine, Roberge & Dalgarno 1983); and (3) H_2 is reformed quickly, in perhaps just ~ 10 yrs at a hydrogen number density $n_H > 10^8 \text{ cm}^{-3}$ (Davis et al. 2002).

SVS 13 also exhibits $[\text{Fe II}]$ emission, which cannot be simply explained by either a HVC associated with the jet, or an LVC. The measured velocity of $\sim -130 \text{ km s}^{-1}$ is remarkably higher than the H_2 HVC and also of that measured in HH 7–10 (-40 to -90 km s^{-1}), while it is lower than that measured in HH 11 (-180 to -200 km s^{-1} — Solf & Böhm 1987; Hartigan et al. 1987; Movsessian et al. 2000). The $[\text{Fe II}]$ emission could originate from a

higher velocity “spine” bracketed within the H₂ jet at a lower velocity, as suggested for the extended jets (Davis et al. 2003). However, our results in §3.1 suggest that the offset of the [Fe II] emission from the star decreases as the velocity increases. This trend is the opposite of what is generally seen in optical observations of outflowing gas from T Tauri stars (see e.g., Takami et al. 2001; Whelan et al. 2004). Based on preliminary proper motion studies, Davis et al. (2006) postulate that the [Fe II] emission at the base of SVS 13 might be excited in a stationary collimated shock in the jet. More detailed spatial information is thus necessary to conclude the nature of the [Fe II] emission associated with SVS 13.

5.2. The Driving Mechanism of the Jet

Understanding the mechanism which drives jets from YSOs is one of the most important key issues for star formation. Radiation and thermal pressure are not sufficient to explain their momentum (see Reipurth & Bally 2001), and there is growing evidence that these flows are magneto-hydrodynamically driven. Possible mechanisms include: magneto-centrifugal force (e.g., Blandford & Payne 1982; Shu et al. 2000; Königl & Pudritz 2000), magnetic pressure (e.g., Uchida & Shibata 1985) and magnetic stress (e.g., Hayashi et al. 1996; Goodson et al. 1999).

Among these magneto-centrifugal wind models seem the most promising. According to these models, magnetic and centrifugal forces act together to launch the jet/wind along magnetic field lines, either from a narrow region of the disk at ≤ 0.1 AU (“X-wind” — see Shu et al. 2000) or from 0.1 to a few tens of AU (“disk wind” — see, e.g., Königl & Pudritz 2000; Ferreira 1997). The magnetic field lines act as solid wires up to the “Alfvén surface”, located at less than 20 AU from the disk. These accelerate the flow particles outwards and upwards in a ‘bead-on-a-wire’ fashion, simultaneously removing angular momentum from the accretion disk. Although present high-resolution facilities cannot resolve the kinematics of the innermost region, the models seem to explain some key observed properties, including the observed mass ejection per mass accretion rates (~ 0.1 , see e.g., Calvet 1997; Richer et al. 2000), and jet motion consistent with rotation around the axis (Davis et al. 2000; Bacciotti et al. 2002; Coffey et al. 2004; Woitas et al. 2005), and in the same sense as the circumstellar disk or molecular envelope (Wiseman et al. 2001; Testi et al. 2002).

To date several authors have accepted the challenge of modelling the forbidden line profiles of T Tauri stars based on magneto-centrifugal wind models, using both X-wind (Shang, Shu, & Glassgold 1998) and disk-wind models (e.g., Cabrit et al. 1999; Pesenti et al. 2003). However, these models do not reproduce well the blueshifted peaks at high and low velocities (see e.g., Shang et al. 1998; Cabrit et al. 1999) and the line profiles are very

different from the observed ones (see e.g., Garcia et al. 2001). Pesenti et al. (2003) attempted in reproducing the two blueshifted [Fe II] $1.644 \mu\text{m}$ emission peaks of L1551-IRS5 observed by Pyo et al. (2002). However, the LVC modelled by these authors has a remarkably smaller spatial scale and higher velocity than observed. In addition, a model by the same authors does not well reproduce the kinematic structure of [Fe II] emission in DG Tau. While the observed line profile clearly shows a separated blueshifted peak at a low velocity ($\sim 100 \text{ km s}^{-1}$) of the position-velocity diagram (Pyo et al. 2003), this is marginal in their DG Tau model.

Unlike forbidden line emission from T Tauri stars, the [Fe II] emission presented here for B5-IRS and HH 34 IRS does not show a low velocity peak. Regarding this point, the P-V diagrams obtained for these objects are similar to those of [S II] emission modelled by Shang et al. (1998), and also the [Fe II] emission modelled for DG Tau by Pesenti et al. (2003). Nevertheless, these two models have significant differences. That of Shang et al. (1998), which is based on the X-wind scenario, shows clear redshifted emission at the base of the flow despite obscuration of the redshifted lobe by a circumstellar disk. This redshifted component has a velocity range similar to the blueshifted side in their model P-V diagrams due to a wide opening angle and perhaps flow rotation in the accelerating region. Pesenti et al. (2003) base their models on disk-winds and in contrast to Shang et al. (1998), do not produce such redshifted emission in their P-V diagrams, exhibiting a sharp intensity ‘cut-off’ near the zero velocity. In Figures 2 and 3, [Fe II] emission in B5-IRS 1 and HH 34 IRS do not show the redshifted emission predicted by Shang et al. (1998). Our results thus support disk-wind models as a driving mechanism for jets, bringing us to the same conclusion as that arrived at for jets in T Tauri stars (Bacciotti et al. 2002; Anderson et al. 2003; Coffey et al. 2004; Woitas et al. 2005).

5.3. Origin of the Low Velocity Component

As described in Sect 5.1, outflowing gas near T Tauri stars and Class I protostars show two velocity components at high and low velocities. While the origin of the HVC is well understood, that of the LVC is still debated. Historically, a hollow-cone flow geometry was first used to explain the two peaks (Appenzeller et al. 1984; Edwards et al. 1987; Ouyed & Pudritz 1993). This has been replaced by the concept that the two components are the result of a combination of different flows, e.g. stellar and disk-winds (e.g., Kwan & Tademaru 1987, 1993); X-wind and disk-wind (Pyo et al. 2002); a reconnection wind and a disk-wind (Pyo et al. 2003). These easily explain the different electron densities and ionizations found for the two velocity components (e.g., Hamann 1994; Hartigan et al. 1995; Hirth et al. 1997). In

contrast, Calvet (1997) shows that the forbidden line luminosities of the LVC are correlated with those of the HVC, suggesting that these two components are intimately related. This is corroborated by the *HST* observations of Bacciotti et al. (2000), who reveal a continuous bracketing of central high velocity gas within a lower velocity, less collimated, broader flow, down to the lowest velocity scales in DG Tau.

Adaptive optics observations by Pyo et al. (2003) show that the velocity of the LVC in DG Tau increases with distance: -60 to -120 km s^{-1} at $0.2''$ to $0.7''$ from the star. If this is due to acceleration, the spatial scale for this acceleration is at least 10–100 times larger than that predicted by models (see e.g., Shu et al. 1994; Ferreira et al. 1997). Pyo et al. (2003) suggest that a significant part of the LVC is not the ejecta of a magneto-hydrodynamically driven wind but gas entrained by the HVC, i.e., a collimated jet.

The H_2 -LVC in B5-IRS 1 exhibits faint extended emission, in which the velocity increases with distance: — $V_{LSR} = -2$ and -20 km s^{-1} at the driving source and $2''$ away, respectively. The “acceleration” occurs over 500 AU, again, much larger than predicted by magneto-hydrodynamical models. This suggests that the faint and extended H_2 emission in B5-IRS 1 is due to entrainment of surrounding gas by a faster flow. As described above, Pyo et al. (2003) argue that the entrainment of the LVC in DG Tau results from interaction with a collimated jet. However, [Fe II] and H_2 observations by Davis et al. (2001, 2003) suggest that such entrainment produces an H_2 velocity similar to, but slightly lower than that of the [Fe II] emission. Thus, it is more likely that the faint H_2 component of B5-IRS 1 is entrained by a slower flow component, i.e., a wide-angled component surrounding the collimated jet. The presence of such an unseen component is indeed predicted by models (see e.g., Cabrit et al. 1999; Shang et al. 2002) and suggested by observations, including the detection of H_2 emission in cavity walls (Davis et al. 2002; Saucedo et al. 2003).

It is not clear whether the remaining component, i.e., the bright peak of H_2 -LVC is also explained by entrainment. Bacciotti et al. (2002) detect internal flow motion for the LVC in DG Tau, and their results agree with rotation as predicted by magneto-centrifugal models. This is corroborated by Takami et al. (2004), who show that H_2 emission in DG Tau is well explained by an outer extension of the kinematic structure predicted by magneto-centrifugal models. High-resolution spectro-imaging of the LVC and proper motion studies could give more crucial constraints on the nature of this component (e.g., Davis et al. 2006).

5.4. Episodic Mass Ejection and Optical Outbursts in SVS 13

HH objects represent fossil records of mass ejection from YSOs. The spatial structure of blueshifted and redshifted jet knots and bow shocks often show near-perfect symmetry, indicating that mass ejection from HH driving sources is episodic (see Reipurth & Bally 2001, and references therein). Some authors argue that this results from episodic mass accretion, observed in extreme cases, as FU Orionis (FUor) or EX Orionis (EXor) outbursts (e.g., Dopita 1978; Reipurth 1989; Herbig 1989).

To date, a dozen YSOs are known as FUor objects. During an optical outburst the brightness of the YSO increases by roughly 5 mag on timescales ranging from less than a year to a decade or more. This has been successfully modelled as an eruptive accretion event in a circumstellar disk with an extremely high mass accretion rate ($\sim 10^{-4} M_{\odot} \text{ yr}^{-1}$ — see e.g., Hartmann & Kenyon 1985). Two scenarios have been proposed to date as a trigger for FUor outbursts: (1) a runaway instability regulated by the ionization of hydrogen in the inner disk (Bell & Lin 1994; Bell et al. 1995), or, (2) disk perturbations caused by a companion star in a highly eccentric orbit (Bonnell & Bastien 1992; Clarke & Syer 1996).

There is growing evidence that FUor eruptions are a standard, albeit infrequent phenomenon of the earliest phases of star formation. Kenyon et al. (1990) show that the number of FUor outbursts observed within 1 kpc of the Sun in the last 50 yrs is much larger than the estimated star formation rate within the same region. Muzerolle et al. (1998) and Calvet et al. (2000) show that the steady disk accretion rate measured using $\text{Br}\gamma$ emission is responsible for only a tiny fraction (0.01–0.1) of the final stellar mass. In addition, Muzerolle et al. (1998) suggest that the typical envelope infall rate onto the accretion disk is 10–100 times larger than the disk accretion rate. This suggests the presence of episodic and violent disk accretion onto the star. Based on the results described above, Kenyon et al. (1990) estimate that each YSO experiences about 10 FUor bursts during its evolution. These most likely occur during the Class I or early Class II phase as all known FUors are associated with reflection nebulae analogous to these protostars (Goodrich 1987), and, submillimetre observations reveal that FUors have accretion disks comparable in mass to Class I protostars (Sandell & Weintraub 2001).

In addition to FUors, there are also a substantial number of stars, namely “EX Ori” (EXor) objects, which undergo more modest and repeatable bursts (Herbig 1989). While the high brightness of FUors lasts several decades or even more, EXor bursts remain at maximum for only a few hundred days. In addition, these two kinds of bursts exhibit remarkably different spectra. Those of FUors do not contain many emission features and have weak $\text{H}\alpha$ emission with very deep and broad blueshifted absorption (see e.g., Hartmann & Calvet 1995). In contrast, the spectra of EXors show a rich variety of emission lines similar

to classical T Tauri stars. Even so, it is likely that both the FUor and EXor bursts result from episodic and violent disk accretion (see e.g., Hartmann, Kenyon, & Hartigan 1993).

Among the objects we observed, SVS 13 underwent an optical outburst about 10 yrs ago, in 1988–1990 (Eisloffel et al. 1991; Mauron & Touvenot 1991), with V and R magnitudes increasing by up to 3 mag. Optical spectra exhibited bright emission lines even after the burst, suggesting that the burst is of the EXor variety rather than FUor (Eisloffel et al. 1991), although the burst continued for at least 500 days (Aspin & Sandell 1994), longer than the previously mentioned typical time scale for an EXor burst (Herbig 1989).

The observed outflow structure in SVS 13 could provide an excellent opportunity to investigate the relationship between optical outbursts and episodic mass ejection. Figure 2 shows three peaks in the H_2 2.122 μm and [Fe II] 1.644 μm emission of SVS 13. These are: (1) an emission knot in the H_2 -HVC, peaking at 1.3'' from the object and with a radial velocity of $\sim -80 \text{ km s}^{-1}$; (2) the H_2 -LVC, peaking at 0.2'' from the star and with a radial velocity of $\sim -30 \text{ km s}^{-1}$; (3) the [Fe II] component, which is offset 0.1'' from the star and has a velocity of -140 km s^{-1} . The dynamical ages of these structures are 30–60, 10–30 and 1–3 yr, respectively, assuming the same inclination angle to the plane of the sky as the extended jet (20–40° — Appendix A). The dynamical age of the knot in the H_2 jet suggests that it predates any episodic mass accretion/ejection event associated with the 1988-1990 optical burst. In contrast, the age of the H_2 low-velocity component does match the time of the burst.

Moreover, recent proper motion measurements suggest that the knot in the H_2 jet moves much more slowly than expected from its radial velocity (Davis et al. 2006). This would suggest an even large dynamical age than 30–60 yrs. In any event further measurements are required for a better determination of the dynamical age, hence enabling a more detailed investigation of the relation (if any) between the ejection and optical burst events.

6. Conclusions

We detect a number of infrared H_2 and [Fe II] lines towards three Herbig-Haro driving sources: SVS 13, B5-IRS 1 and HH 34 IRS. These line include H_2 transitions with $v=1-3$ and $J=1-11$, and several [Fe II] lines with upper energy levels $E/k = 1.1 - 2.7 \times 10^4 \text{ K}$. Outflowing gas in all objects show the presence of two blueshifted components at high (-70 to -130 km s^{-1}) and low velocities (-10 to -30 km s^{-1}), characteristically similar to forbidden line emission associated with T Tauri stars but without a low velocity peak for the forbidden lines, which is observed in the H_2 emission. In SVS 13, the HVC also appears in H_2 emission.

This reflects the low-excitation nature of the outflowing gas close to these HH driving sources.

The observed H₂ flux ratios indicate a temperature and density of $2 - 3 \times 10^3$ K and $\geq 10^5$ cm⁻³, respectively. In particular the temperature obtained from the $I_{2-1S(1)}/I_{1-0S(1)}$ ratio remains quite constant at 2×10^3 K, lending support to shock heating for the excitation of the gas. In the jet of SVS 13, the gas density is seen to decrease further downstream. The observed level population of H₂ indicates a hydrogen number density $n_H > 10^5 - 10^8$ cm⁻³ depending on whether the excitation is dominated by H-H₂ or H₂-H₂ collisions, respectively. The observed electron density and temperature in [Fe II] emission line regions are $\sim 10^4$ cm⁻³ or greater, similar to FEL regions associated with T Tauri stars.

The absence of an LVC in [Fe II] emission in all three HH driving sources matches models based on magneto-centrifugal winds. Our results in B5-IRS 1 and HH 34 IRS so far support disk-wind models, which predict that the jet/wind originates from the disk surface at radii of a few AU. Currently the X-wind model, which predicts that the jet/wind originates from the inner disk edge within 0.1 AU of the star, cannot explain the absence of redshifted emission at the driving source. More detailed information regarding jet launching could be extracted if accurate collisional rate coefficients for [Fe II] ²P states are obtained. In B5-IRS 1 the faint extended component of H₂-LVC slowly accelerates over a large spatial scale (~ 20 km s⁻¹ at ~ 500 AU). We suggest that the emission is due to interaction between a slow and unseen wide-angled wind and the surrounding ambient gas.

We thank an anonymous referee for useful comments. We acknowledge the data analysis facilities provided by the Starlink Project which is run by CCLRC on behalf of PPARC. MT thanks PPARC for support through a PDRA up until September 2004. TPR acknowledges support from Science Foundation Ireland through contract 04/BR6/PO2741. This research has made use of the Simbad database, operated at CDS, Strasbourg, France, and of the NASA’s Astrophysics Data System Abstract Service.

Facilities: Subaru (IRCS).

A. Notes on Targets

A.1. SVS 13

SVS 13 is the driving source of the HH 7–11 outflow, which extends to the southeast for over an arcminute (see e.g. Bachiller et al. 2000). The parent star-forming region, NGC 1333, lies between 220 and 350 pc away (Herbig & Jones 1983; Cernis 1990; de Zeeuw et al. 1999).

For this work, we adopt a distance to SVS 13 of 300 pc. Analysis of the radial and proper motions of the atomic line emission from HH 7–10 yield radial velocities of $40 - 90 \text{ km s}^{-1}$ (Solf & Böhm 1987; Hartigan et al. 1987; Movsessian et al. 2000) and tangential velocities of $20 - 60 \text{ km s}^{-1}$ ($0.015'' - 0.044'' \text{ yr}^{-1}$ — Noriega-Crespo & Garnavich 2001; Khanzadyan et al. 2003). Based on Noriega-Crespo & Garnavich (2001) and adopted distance of 300 pc, we estimate an outflow angle to the line of sight of $20^\circ - 40^\circ$. The inner knot HH 11 possess a much higher radial velocity ($180 - 200 \text{ km s}^{-1}$) than HH 7–10, suggesting that it is generated by a relatively recent high-speed outburst (Solf & Böhm 1987). SVS 13 exhibited a large increase of its brightness in the optical and near-IR in 1988–1990 (by 2.5–3.4 and 1–2 mag., respectively — Eislöffel et al. 1991; Maun & Thouvenot 1991; Liseau, Lorenzetti & Molinari 1992). VLA observations by Anglada (2000) revealed two components in the E-W direction separated by $0.3''$, indicating that SVS 13 is a close binary system.

The presence of near-IR H_2 emission at SVS 13 itself was first reported by Carr (1990). H_2 and [Fe II] emission in the extended outflow HH 7–11 have been observed for decades by a number of authors (Zealey, Williams & Sandel 1984, Garden, Russell & Burton 1990, Stapelfeldt et al. 1991, Carr 1993, Fernandes & Brand 1995, Gredel 1996; Everett 1997, Chrysostomou et al. 2000; Davis et al. 2000, 2001, 2002 and Khanzadyan et al. 2003 for H_2 ; Stapelfeldt et al. 1991 and Everett 1997 for [Fe II]).

A.2. B5-IRS 1

This protostar drives a parsec-scale, jet-like, bipolar HH flow HH 366 which extends in an east-west direction (Bally et al. 1996). Bally et al. (1996) shows that the outflow extends for about $22'$, corresponding to a projected length of about 2.2 pc, and $\text{H}\alpha$ and [SII] lines reveal radial velocities of -30 to -10 km s^{-1} and 35 to 90 km s^{-1} for the eastern and western chains respectively. Yu et al. (1999) derive an inclination angle of 77° to the line of sight from the projected size and velocity extent of the associated molecular outflow. The parent dark cloud Barnard 5 is located at the eastern end of the Perseus molecular cloud complex, which also include NGC 1333 and SVS 13. We then adopt the same distance as SVS 13: that is, 300 pc. The presence of H_2 and [Fe II] emission at the driving source was first revealed by Reipurth & Aspin (1997) and Davis et al. (2003), respectively.

A.3. HH 34 IRS

The HH 34 IRS is responsible for a number of HH objects in an north-south direction extending over $21'$. These include HH 34S/N/X, HH 40, HH 85–88, HH 126, and HH 173 (Bally & Devine 1994; Devine et al. 1997). The object also exhibit a well collimated jet extending towards the south with a spatial scale of $\sim 20''$ (Reipurth et al. 1986, 2000, 2002; Bührke et al. 1988; Ray et al. 1996). Eislöffel & Mundt (1992) and Heathcote & Reipurth (1992) derive a inclination angle of 23° – 28° to the line of the sight, based on their proper motion measurements and radial velocities in the literature. HH 34 IRS is much less embedded than the other Class I protostars ($A_V \sim 5$), and its spectrum at optical wavelengths is rich in emission lines like classical T Tauri stars (Reipurth et al. 1986). Estimates of the distance to the parent SFR (Orion OB1 association) span the range 400–500 pc (see, e.g., Warren & Hesser 1978; Genzel & Stutzki 1989). We adopt a distance of 450 pc in this paper. Near-IR H_2 and [Fe II] emission within a few arcsec of this object was first observed by Reipurth & Aspin (1997) and Reipurth et al. (2000), respectively.

B. Positional Differences between H - and K -Band Continuum

Since H - and K -band spectra were obtained with different exposures, the spatial structure of emission lines between the two bands cannot be compared unless their relative position is determined. Class I protostars are often heavily embedded ($A_V \sim 50$ mag — Whitney et al. 1997), and we usually see scattered light even in the H - and K -bands. This causes a positional difference between the two bands due to different scattering geometries and optical depths (see e.g., Weintraub, Kastner & Whitney 1995). To determine the relative position of H - and K -band continuum emission we obtained exposures in these bands using the imaging mode of IRCS. The continuum positions for each object were then measured using other stars in the same field of view. We find that, in B5-IRS1, the position of the H -band continuum is located at $\sim 0.06''$ east of the K -band continuum, in the same direction as the blueshifted knot HH 365-E. This trend is what we expect due to different scattering geometries between these two bands (see Weintraub et al. 1995). No positional differences exceeding $0.03''$ (0.5 pixel) are measured in the other objects. Since the measured positional difference is much smaller than the seeing ($0.6''$), we thus performed comparisons between the two bands without correcting for these positional differences.

REFERENCES

- Anderson, J. M., Li, Z., Krasnopolsky, R., & Blandford, R. D. 2003, *ApJ*, 590, L107
- Anglada, G., Rodríguez, L. F., & Torrelles, J. M. 2000, *ApJ*, 542, L123
- Appenzeller, I., Oestreicher, R., & Jankovics, I. 1984, *A&A*, 141, 108
- Aspin, C., & Sandell, G. 1994, *A&A*, 288, 803
- Bacciotti, F., & Eisloffel, J. 1999, *A&A*, 342, 717
- Bacciotti, F., Mundt, R., Ray, T. P., Eisloffel, J., Solf, J., & Camezind, M. 2000, *ApJ*, 537, L49
- Bacciotti, F., Ray, T. P., Mundt, R., Eisloffel, J., & Solf, J. 2002, *ApJ*, 576, 222
- Bachiller, R., Gueth, F., Guilloteau, S., Tafalla, M., & Dutrey, A. 2000, *A&A*, 362, L33
- Bally, J., & Devine, D. 1994, *ApJ*, 428, L65
- Bally, J., Devine, D., & Alten, V. 1996, *ApJ*, 473, 921
- Bautista, M. A., & Pradhan, A. K. 1998, *ApJ*, 492, 650
- Bell, K. R., & Lin, D. N. C. 1994, *ApJ*, 427, 987
- Bell, K. R., Lin, D. N. C., Hartmann, L. W., & Kenyon, S. J. 1995, *ApJ*, 444, 376
- Blandford, R. D., & Payne, D. G. 1982, *MNRAS*, 199, 883
- Bonnell, I., & Bastien, P. 1992, *ApJ*, 401, L31
- Brand, P. W. J. L., Moorhouse, A., Burton, M. G., Geballe, T. R., Bird, M., & Wade, R. 1988, *ApJ*, 334, L103
- Bührke, T., Mundt, R., & Ray, T. P. 1988, *A&A*, 200, 99
- Burton, M. G., Brand, P. W. J. L., Geballe, T. R., & Webster, A. S. 1989, *MNRAS*, 236, 409
- Burton, M. G., Hollenbach, D. J., & Tielens, A. G. G. M. 1990, *ApJ*, 365, 620
- Cabrit, S., Ferreira, J., & Raga, A. C. 1999, *A&A*, 343, L61
- Calvet, N. 1997, *IAU Symp. 182: Herbig-Haro Flows and the Birth of Stars*, 182, 417

- Calvet, N., Hartmann, L., & Strom, S. E. 2000, *Protostars and Planets IV*, ed. V. Mannings, A. P. Boss, & S. S. Russell (Tucson: Univ. Arizona Press), 377
- Carr, J. S. 1990, *AJ*, 100, 1244
- Carr, J. S. 1993, *ApJ*, 406, 553
- Carr, J. S., Tokunaga, A. T., & Najita, J. 2004, *ApJ*, 603, 213
- Cernis, K. 1990, *Ap&SS*, 166, 315
- Chernin, L. M., & Masson, C. R. 1995, *ApJ*, 443, 181
- Chrysostomou, A., Hobson, J., Davis, C. J., Smith, M. D., & Berndsen, A. 2000, *MNRAS*, 314, 229
- Clarke, C. J., & Syer, D. 1996, *MNRAS*, 278, L23
- Coffey, D., Bacciotti, F., Woitas, J., Ray, T. P., & Eislöffel, J. 2004, *ApJ*, 604, 758
- Davis, C. J., Berndsen, A., Smith, M. D., Chrysostomou, A., & Hobson, J. 2000, *MNRAS*, 314, 241
- Davis, C. J., Nisini, B., Takami, M., Pyo, T.S., Smith, H.D., Whelan, E., Ray, T. P., & Chrysostomou, A. 2006, *ApJ*, in press
- Davis, C. J., Stern, L., Ray, T. P., & Chrysostomou, A. 2002, *A&A*, 382, 1021
- Davis, C. J., Ray, T. P., Desroches, L., & Aspin, C. 2001, *MNRAS*, 326, 524
- Davis, C. J., Whelan, E., Ray, T. P., & Chrysostomou, A. 2003, *A&A*, 397, 693
- Devine, D., Bally, J., Reipurth, B., & Heathcote, S. 1997, *AJ*, 114, 2095
- Devine, D., Bally, J., Reipurth, B., & Heathcote, S. 1997, *AJ*, 114, 2095
- de Zeeuw, P. T., Hoogerwerf, R., de Bruijne, J. H. J., Brown, A. G. A., & Blaauw, A. 1999, *AJ*, 117, 354
- Dopita, M. A. 1978, *ApJS*, 37, 117
- Dougados, C., Cabrit, S., & Lavalley-Fouquet, C. 2002, *Revista Mexicana de Astronomia y Astrofisica Conference Series*, 13, 43
- Draine, B. T., Roberge, W. G., & Dalgarno, A. 1983, *ApJ*, 264, 485

- Edwards, S., Cabrit, S., Strom, S. E., Heyer, I., Strom, K. M., & Anderson, E. 1987, *ApJ*, 321, 473
- Eislöeffel, J., Guenther, E., Hessman, F. V., Mundt, R., Poetzel, R., Carr, J. S., Beckwith, S., & Ray, T. P. 1991, *ApJ*, 383, L19
- Eislöeffel, J., & Mundt, R. 1992, *A&A*, 263, 292
- Eislöeffel, J., Mundt, R., Ray, T. P., & Rodríguez, L. F. 2000a, *Protostars and Planets IV*, ed. V. Mannings, A. P. Boss, & S. S. Russell (Tucson: Univ. Arizona Press), 815
- Eislöeffel, J., Smith, M. D., & Davis, C. J. 2000b, *A&A*, 359, 1147
- Everett, M. E. 1997, *ApJ*, 478, 246
- Everett, M. E., Depoy, D. L., & Pogge, R. W. 1995, *AJ*, 110, 1295
- Fernandes, A. J. L., & Brand, P. W. J. L. 1995, *MNRAS*, 274, 639
- Ferreira, J. 1997, *A&A*, 319, 340
- Garcia, P. J. V., Cabrit, S., Ferreira, J., & Binette, L. 2001, *A&A*, 377, 609
- Garden, R. P., Russell, A. P. G., & Burton, M. G. 1990, *ApJ*, 354, 232
- Genzel, R., & Stutzki, J. 1989, *ARA&A*, 27, 41
- Giannini, T., Nisini, B., Caratti o Garatti, A., & Lorenzetti, D. 2002, *ApJ*, 570, L33
- Goodrich, R. W. 1987, *PASP*, 99, 116
- Goodson, A. P., Böhm, K., & Winglee, R. M. 1999, *ApJ*, 524, 142
- Gredel, R. 1994, *A&A*, 292, 580
- Gredel, R. 1996, *A&A*, 305, 582
- Hamann, F. 1994, *ApJS*, 93, 485
- Hamann, F., Simon, M., Carr, J. S., & Prato, L. 1994, *ApJ*, 436, 292
- Hartigan, P., Edwards, S., & Ghandour, L. 1995, *ApJ*, 452, 736
- Hartigan, P., Raymond, J., & Hartmann, L. 1987, *ApJ*, 316, 323
- Hartmann, L., Avrett, E., & Edwards, S. 1982, *ApJ*, 261, 279

- Hartmann, L., & Calvet, N. 1995, *AJ*, 109, 1846
- Hartmann, L., & Kenyon, S. J. 1985, *ApJ*, 299, 462
- Hartmann, L., Kenyon, S., & Hartigan, P. 1993, *Protostars and Planets III*, 497
N., & Miyama, S. M. 1993, *ApJ*, 418, L71
- Hasegawa, T., Gatley, I., Garden, R. P., Brand, P. W. J. L., Ohishi, M., Hayashi, M., & Kaifu, N. 1987, *ApJ*, 318, L77
- Hayashi, M. R., Shibata, K., & Matsumoto, R. 1996, *ApJ*, 468, L37
- Heathcote, S., & Reipurth, B. 1992, *AJ*, 104, 2193
- Herbig, G. H. 1989, in *Proc. ESO Workshop on Low Mass Star Formation and PreMain Sequence Objects*, ed. B. Reipurth (Garching: ESO), 233
- Herbig, G. H., & Jones, B. F. 1983, *AJ*, 88, 1040
& Solf, J. 1994, *A&A*, 285, 929
- Hirth, G. A., Mundt, R., & Solf, J. 1997, *A&AS*, 126, 437
- Hollenbach, D., & McKee, C. F. 1989, *ApJ*, 342, 306
- Itoh, Y., et al. 2000, *PASJ*, 52, 81
- Kenyon, S. J., Hartmann, L. W., Strom, K. M., & Strom, S. E. 1990, *AJ*, 99, 869
- Khanzadyan, T., Smith, M. D., Davis, C. J., Gredel, R., Stanke, T., & Chrysostomou, A. 2003, *MNRAS*, 338, 57
- Kobayashi, N., et al. 2000, *Proc. SPIE*, 4008, 1056
- Königl, A., & Pudritz, R. E. 2000, *Protostars and Planets IV*, ed. V. Mannings, A. P. Boss, & S. S. Russell (Tucson: Univ. Arizona Press), 759
- Knee, L. B. G., & Sandell, G. 2000, *A&A*, 361, 671
- Kwan, J., & Tademaru, E. 1988, *ApJ*, 332, L41
- Kwan, J., & Tademaru, E. 1995, *ApJ*, 454, 382
- Lavalley-Fouquet, C., Cabrit, S., & Dougados, C. 2000, *A&A*, 356, L41
- Liseau, R., Lorenzetti, D., & Molinari, S. 1992, *A&A*, 253, 119

- Maloney, P. R., Hollenbach, D. J., & Tielens, A. G. G. M. 1996, *ApJ*, 466, 561
- Mauron, N., & Thouvenot, E. 1991, *IAU Circ.*, 5261, 2
- Movsessian, T. A., Magakian, T. Y., Amram, P., Boulesteix, J., & Gach, J.-L. 2000, *A&A*, 364, 293
- Muzerolle, J., Hartmann, L., & Calvet, N. 1998, *AJ*, 116, 2965
- Najita, J. R., Edwards, S., Basri, G., & Carr, J. 2000, *Protostars and Planets IV*, ed. V. Mannings, A. P. Boss, & S. S. Russell (Tucson: Univ. Arizona Press), 457
- Natta, A., Giovanardi, C., & Palla, F. 1988, *ApJ*, 332, 921
- Nisini, B., Antonucci, S., & Giannini, T. 2004, *A&A*, 421, 187
- Nisini, B., Caratti o Garatti, A., Giannini, T., & Lorenzetti, D. 2002, *A&A*, 393, 1035
- Noriega-Crespo, A., & Garnavich, P. M. 2001, *AJ*, 122, 3317
- Nussbaumer, H., & Storey, P. J. 1988, *A&A*, 193, 327
- Ouyed, R., & Pudritz, R. E. 1994, *ApJ*, 423, 753
- Pesenti, N., Dougados, C., Cabrit, S., O'Brien, D., Garcia, P., & Ferreira, J. 2003, *A&A*, 410, 155
- Pyo, T., Hayashi, M., Kobayashi, N., Terada, H., Goto, M., Yamashita, T., Tokunaga, A. T., & Itoh, Y. 2002, *ApJ*, 570, 724
- Pyo, T., et al. 2003, *ApJ*, 590, 340
- Pyo, T., et al. 2005, *ApJ*, 618, 817
- Ray, T. P., Mundt, R., Dyson, J. E., Falle, S. A. E. G., & Raga, A. C. 1996, *ApJ*, 468, L103
- Reipurth, B. 1989, *Nature*, 340, 42
- Reipurth, B., & Aspin, C. 1997, *AJ*, 114, 2700
- Reipurth, B., & Bally, J. 2001, *ARA&A*, 39, 403
- Reipurth, B., Bally, J., Graham, J. A., Lane, A. P., & Zealey, W. J. 1986, *A&A*, 164, 51
- Reipurth, B., Heathcote, S., Morse, J., Hartigan, P., & Bally, J. 2002, *AJ*, 123, 362

- Reipurth, B., Yu, K., Heathcote, S., Bally, J., & Rodríguez, L. F. 2000, *AJ*, 120, 1449
- Richer, J. S., Shepherd, D. S., Cabrit, S., Bachiller, R., & Churchwell, E. 2000, *Protostars and Planets IV*, ed. V. Mannings, A. P. Boss, & S. S. Russell (Tucson: Univ. Arizona Press), 867
- Richter, M. J., Graham, J. R., & Wright, G. S. 1995, *ApJ*, 454, 277
- Rieke, G. H., & Lebofsky, M. J. 1985, *ApJ*, 288, 618
- Safier, P. N. 1993, *ApJ*, 408, 115
- Saucedo, J., Calvet, N., Hartmann, L., & Raymond, J. 2003, *ApJ*, 591, 275
- Sandell, G., & Weintraub, D. A. 2001, *ApJS*, 134, 115
- Shang, H., Glassgold, A. E., Shu, F. H., & Lizano, S. 2002, *ApJ*, 564, 853
- Shang, H., Shu, F. H., & Glassgold, A. E. 1998, *ApJ*, 493, L91
- Shu, F., Najita, J., Ostriker, E., Wilkin, F., Ruden, S., & Lizano, S. 1994, *ApJ*, 429, 781
- Shu, F. H., Najita, J. R., Shang, H., & Li, Z.-Y. 2000, *Protostars and Planets IV*, ed. V. Mannings, A. P. Boss, & S. S. Russell (Tucson: Univ. Arizona Press), 789
- Solf, J., & Böhm, K. H. 1987, *AJ*, 93, 1172
- Stapelfeldt, K. R., Scoville, N. Z., Beichman, C. A., Hester, J. J., & Gautier, T. N. 1991, *ApJ*, 371, 226
- Takami, M., Bailey, J., & Chrysostomou, A. 2003, *A&A*, 397, 675
- Takami, M., Chrysostomou, A., Bailey, J., Gledhill, T. M., Tamura, M., & Terada, H. 2002, *ApJ*, 568, L53
- Takami, M., Chrysostomou, A., Ray, T. P., Davis, C., Dent, W. R. F., Bailey, J., Tamura, M., & Terada, H. 2004, *A&A*, 416, 213
- Takami, M., Bailey, J., Gledhill, T. M., Chrysostomou, A., & Hough, J. H. 2001, *MNRAS*, 323, 177
- Tanaka, M., Hasegawa, T., Hayashi, S. S., Brand, P. W. J. L., & Gatley, I. 1989, *ApJ*, 336, 207
- Testi, L., Bacciotti, F., Sargent, A. I., Ray, T. P., & Eisloffel, J. 2002, *A&A*, 394, L31

- Tine, S., Lepp, S., Gredel, R., & Dalgarno, A. 1997, *ApJ*, 481, 282
- Tokunaga, A. T., et al. 1998, *Proc. SPIE*, 3354, 512
- Turner, J., Kirby-Docken, K., & Dalgarno, A. 1977, *ApJS*, 35, 281
- Uchida, Y., & Shibata, K. 1985, *PASJ*, 37, 515
- Valenti, J. A., Johns-Krull, C. M., & Linsky, J. L. 2000, *ApJS*, 129, 399
- Verner, E. M., Verner, D. A., Baldwin, J. A., Ferland, G. J., & Martin, P. G. 2000, *ApJ*, 543, 831
- Verner, E. M., Verner, D. A., Korista, K. T., Ferguson, J. W., Hamann, F., & Ferland, G. J. 1999, *ApJS*, 120, 101
- Warren, W. H., & Hesser, J. E. 1978, *ApJS*, 36, 497
- Weintraub, D. A., Kastner, J. H., & Whitney, B. A. 1995, *ApJ*, 452, L141
- Whelan, E. T., Ray, T. P., & Davis, C. J. 2004, *A&A*, 417, 247
- Whitney, B. A., Kenyon, S. J., & Gomez, M. 1997, *ApJ*, 485, 703
- Wiseman, J., Wootten, A., Zinnecker, H., & McCaughrean, M. 2001, *ApJ*, 550, L87
- Woitas, J., Bacciotti, F., Ray, T. P., Marconi, A., Coffey, D., & Eisloffel, J. 2005, *A&A*, 432, 149
- Woitas, J., Ray, T. P., Bacciotti, F., Davis, C. J., & Eisloffel, J. 2002, *ApJ*, 580, 336
- Yu, K., Billawala, Y., & Bally, J. 1999, *AJ*, 118, 2940
- Zealey, W. J., Williams, P. M., & Sandell, G. 1984, *A&A*, 140, L31
- Zhang, H. L., & Pradhan, A. K. 1995, *A&A*, 293, 953

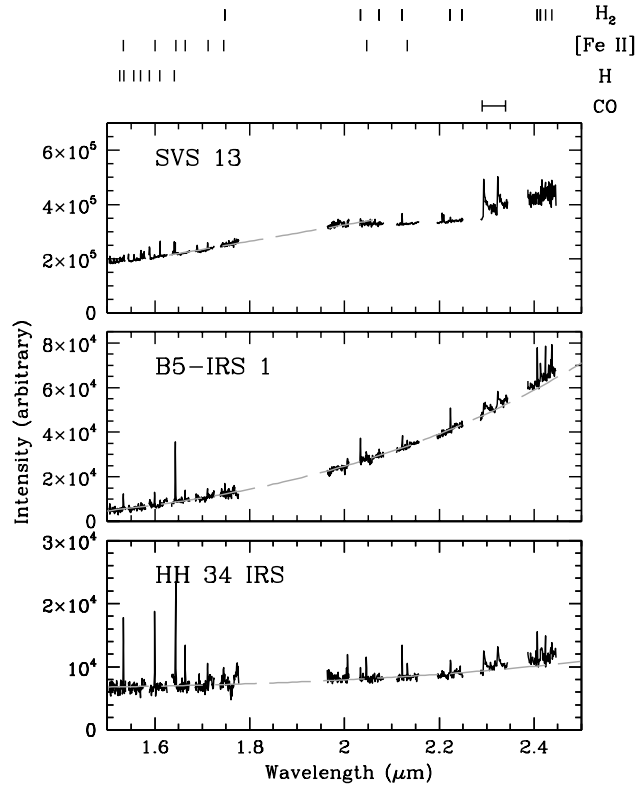


Fig. 1.— Spectra obtained towards SVS 13, B5-IRS 1 and HH 34 IRS. The spectra are binned into 16 pixel bins, providing an actual spectral resolution $R=2500$. Bright emission features are indicated at the top. The grey dashed lines show the continuum level the spectra were scaled to (see text).

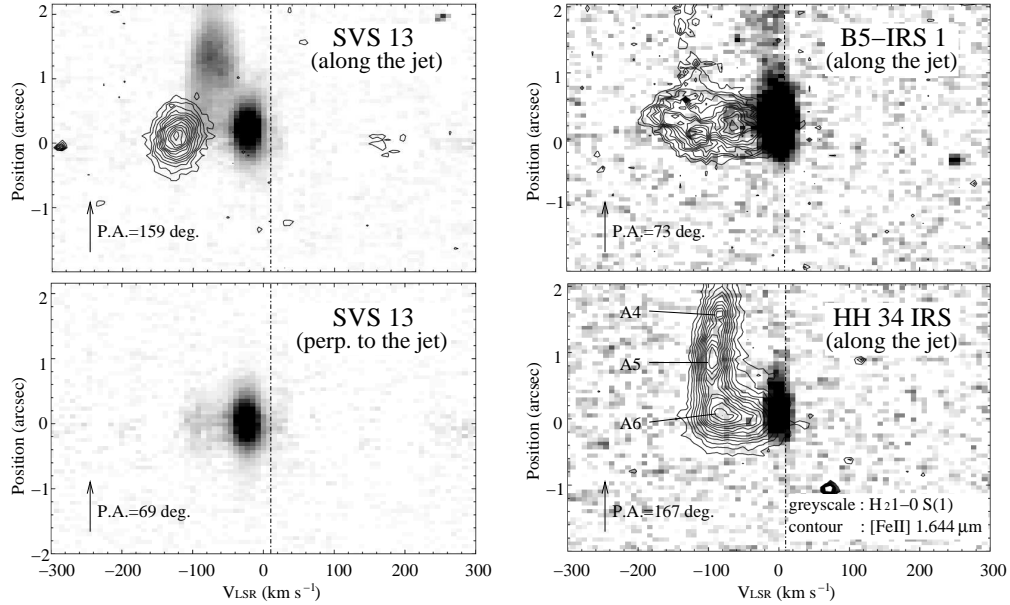


Fig. 2.— Continuum-subtracted position velocity diagrams of H₂ 2.122 μm and [Fe II] 1.644 μm emission. Greyscale and contours show the H₂ and [Fe II] emission, respectively. The contour spacing is 7% of the peak intensity. The dot-dashed line shows the LSR velocity of the parent cloud. The zero spatial position of H₂ and [Fe II] emission corresponds to the continuum centroid position adjacent to each line. The continuum centroid positions at these wavelengths coincide with each other to within an accuracy of 0.1'' in all objects (see Appendix B). The nomenclature for the knots in HH 34 are based on Reipurth et al. (2002). No contours are seen in the lower-left figure since [Fe II] spectra were not obtained at this slit position.

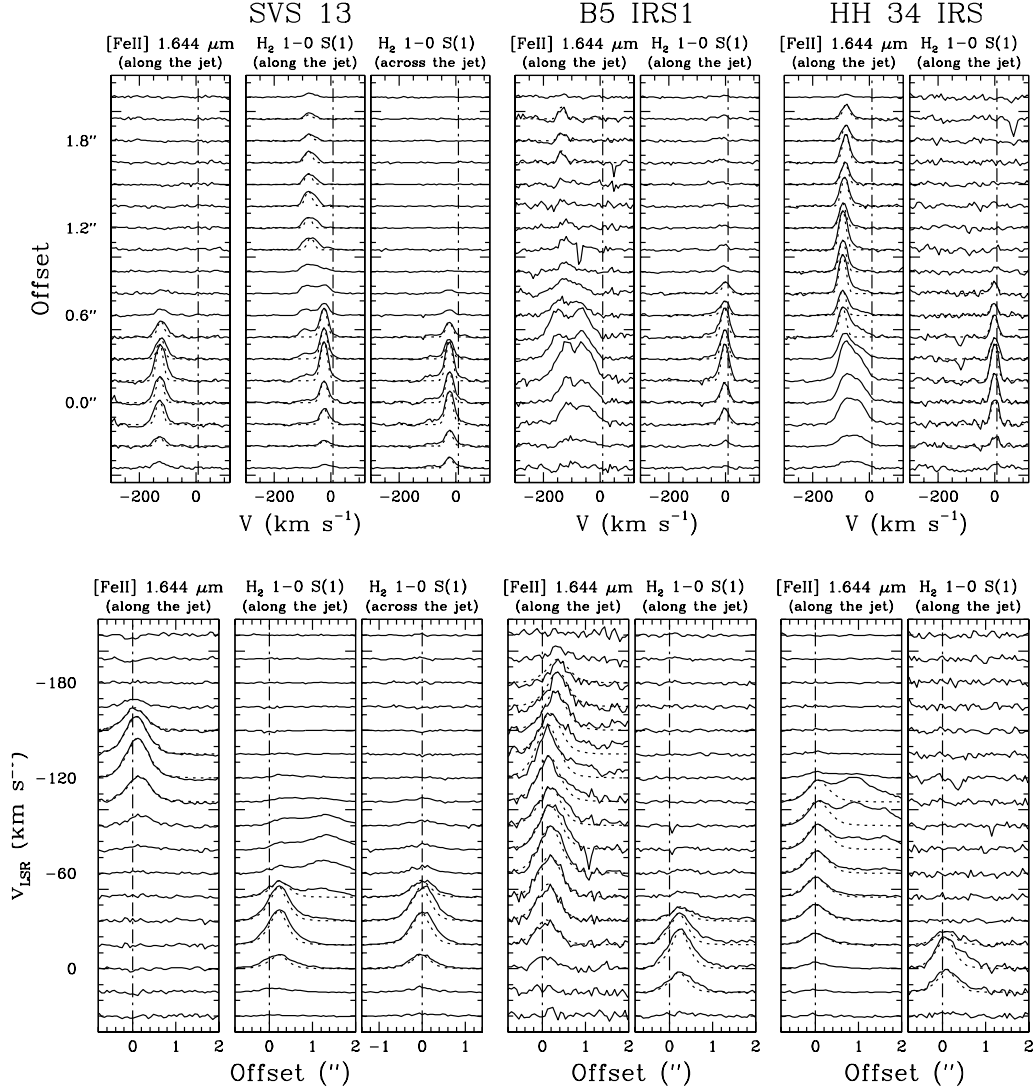


Fig. 3.— (*top*) Line profiles of [Fe II] 1.644 μm and H₂ 1-0 S(1) at individual positional offsets from the star. Dotted curves show the instrumental profile. The dot-dashed lines shows the systemic velocity of the parent cloud. (*bottom*) Intensity distributions of the same lines at given velocities. Dotted curves show the seeing profile. The dot-dashed lines shows the continuum position of the star.

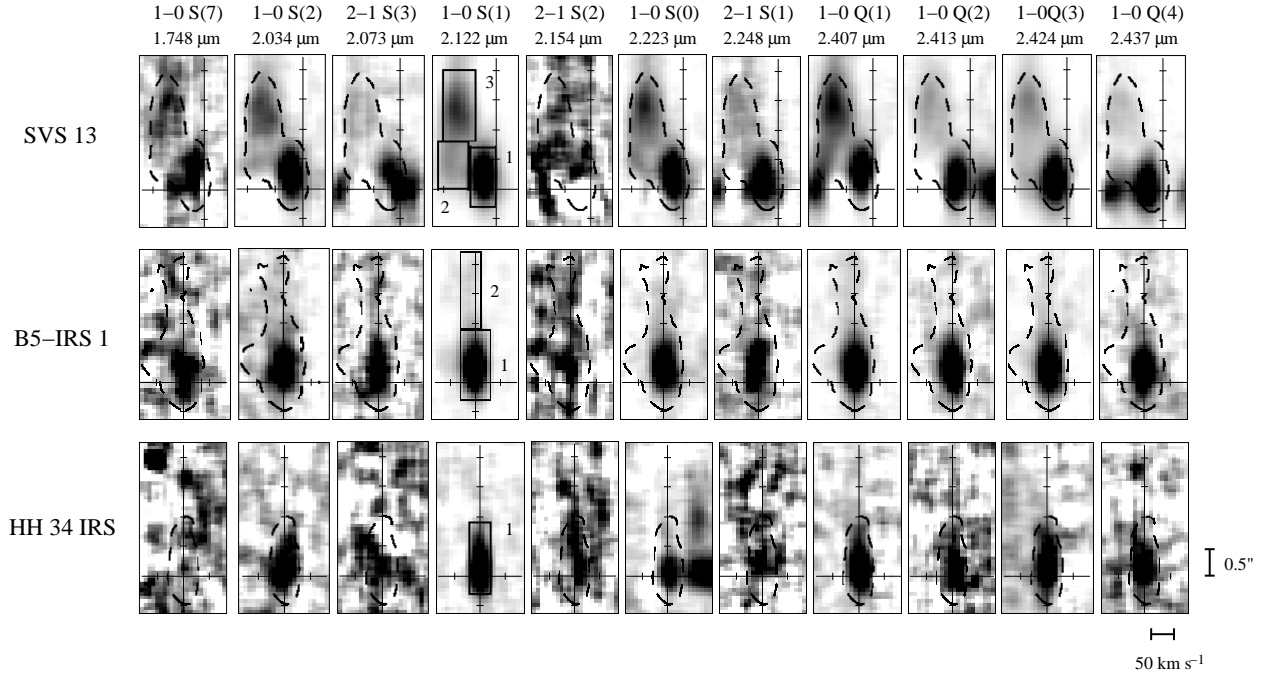


Fig. 4.— Continuum-subtracted position-velocity diagrams of H_2 lines. The greyscale is arbitrarily adjusted for each panel to enhance the faint emission. Dashed curves show a single contour of 1–0 S(1) emission, corresponding to 15, 5, 10% of the peak intensity for SVS 13, B5-IRS 1 and HH 34 IRS, respectively. In the diagram for 1–0 S(1) emission we indicate the regions where the line intensities given in Table 2 are measured. Note that some panels for SVS 13 also contain emission/absorption features at the star. We also see bright emission at positive velocities relative to the 1–0 S(0) line for HH 34 IRS. This is due to either a ghost or an unidentified line associated with the object.

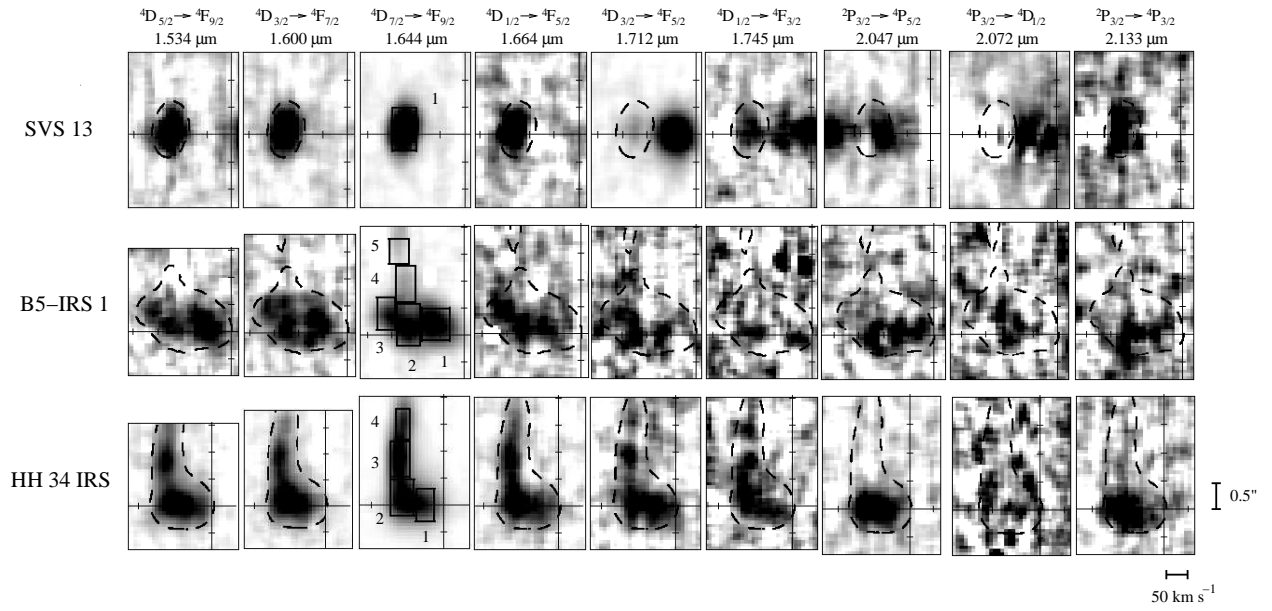


Fig. 5.— The same as Figure 4 but for [Fe II] lines. Dashed curves show a single contour of 1.644 μm emission, corresponding to 20% of the peak intensity. In the diagram for 1.644 μm emission we indicate regions where the line intensities given in Table 2 are measured.

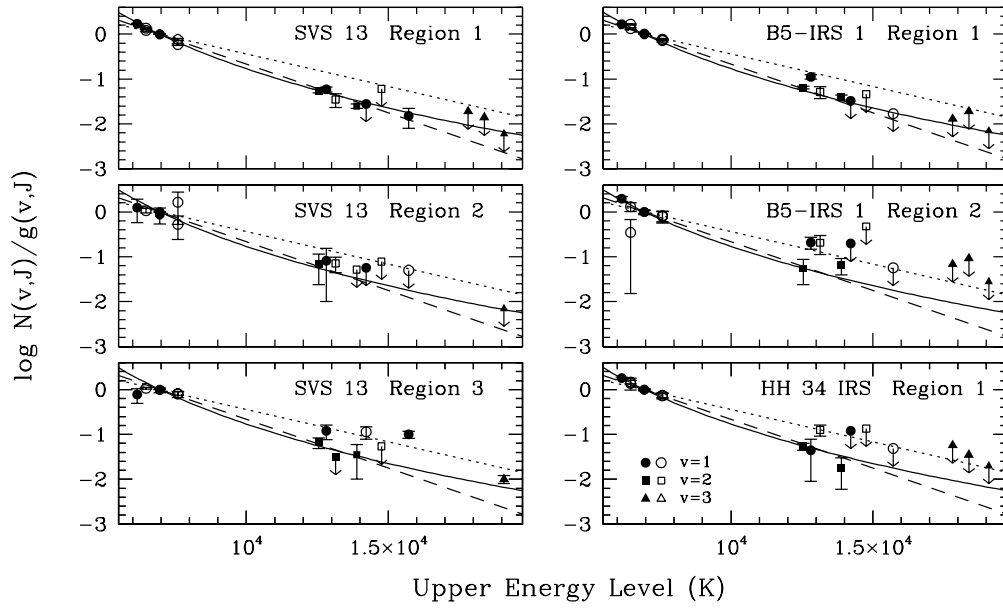


Fig. 6.— Population diagram of H_2 emission for regions shown in Figure 4. Circles, squares and triangles indicate the populations at $v = 1, 2, 3$ respectively. Filled and open marks indicate those for ortho and para H_2 , respectively. Dashed and dotted lines indicate an LTE population at $T=2000$ and 3000 K, respectively. Solid curves show the populations for a dissociative J-shock modelled by Brand et al. (1988).

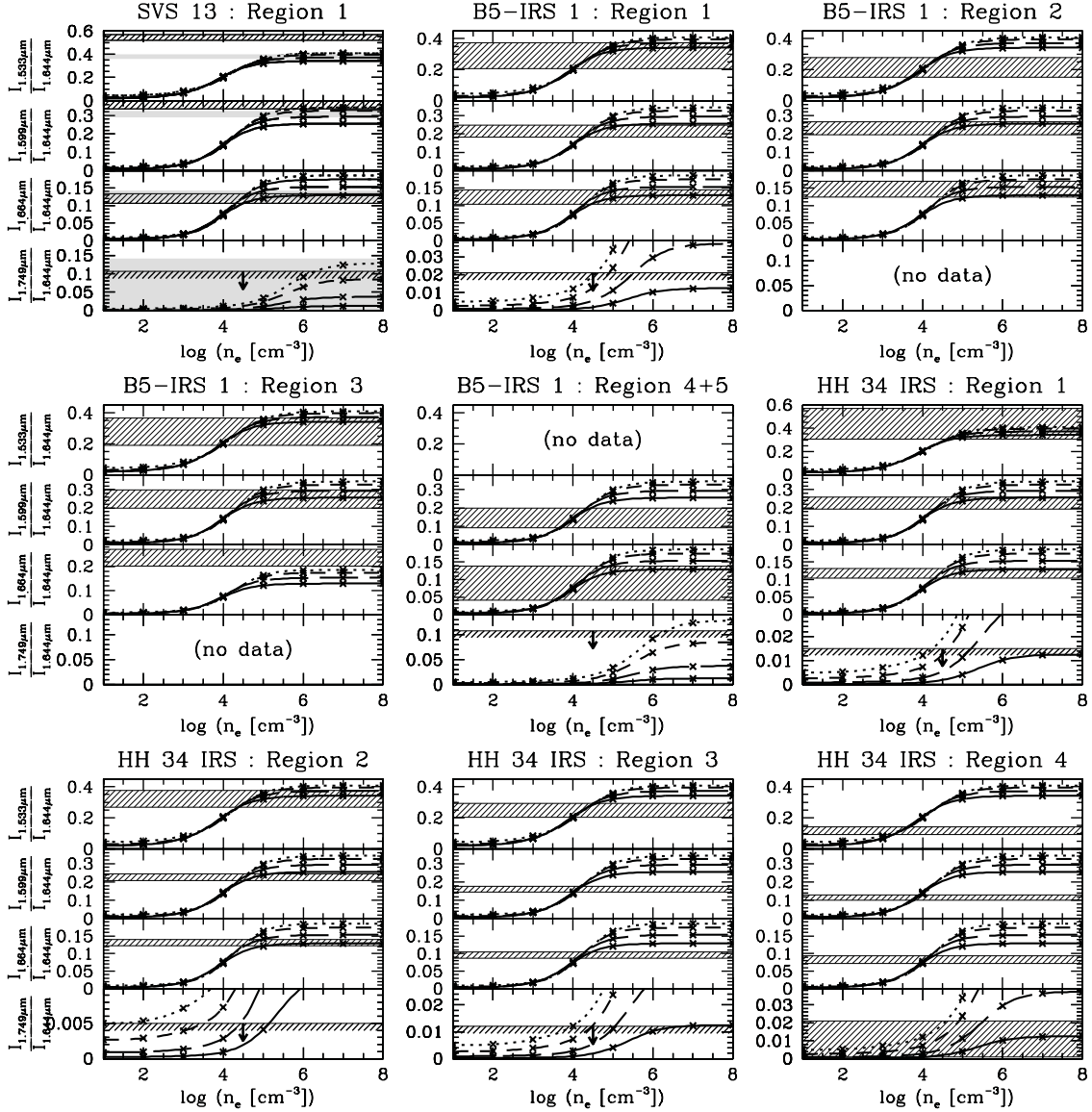


Fig. 7.— Modeled and observed [Fe II] line flux ratios. Modeled values are shown as solid, long-dashed, short dashed and dotted lines for $T_e=0.3/0.5/1/2 \times 10^4$ K, respectively. The hatched regions indicate the observed flux ratios and their uncertainty. For SVS 13, hatched and grey regions show the ratios for $A_V = 20$ and 0, respectively. Upper limits are used for extinction towards the other objects (see Table 5) which is propagated into the observed ratios shown here.

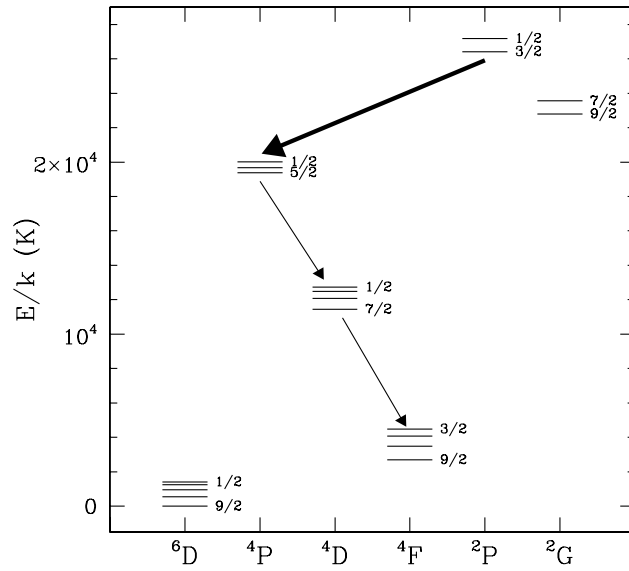


Fig. 8.— Lowest 20 levels of Fe^+ . Arrows show transitions we detect above the 3σ level in at least one of our targets. The thick arrow shows the ${}^2P \rightarrow {}^4P$ transitions.

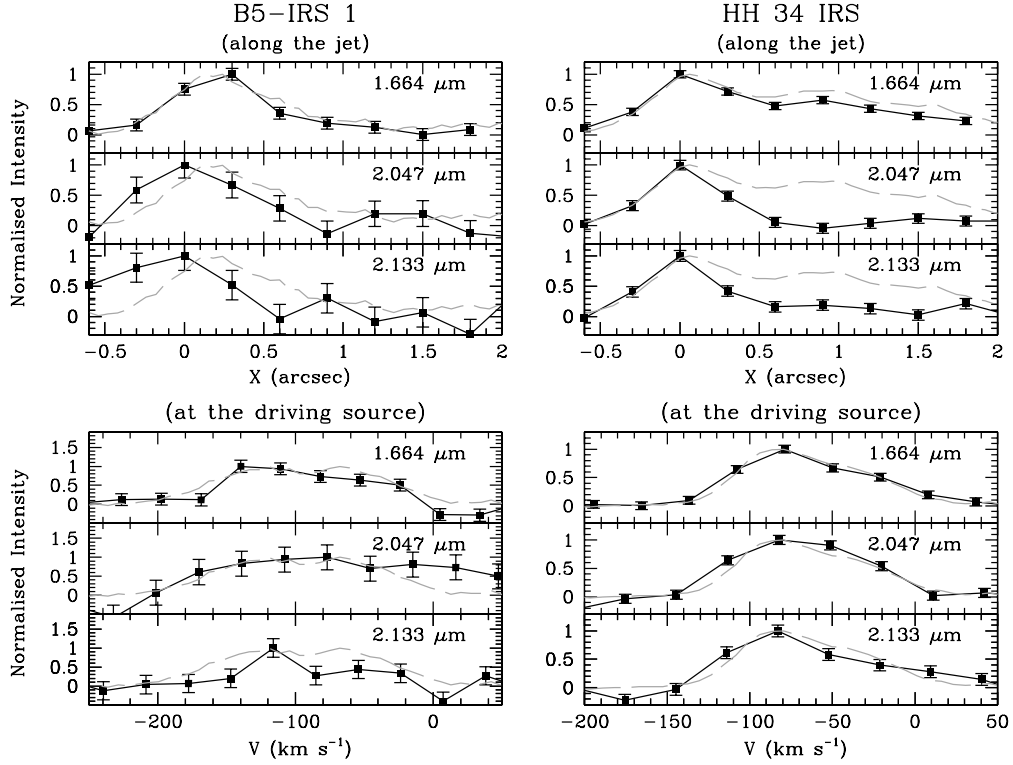


Fig. 9.— Spatial distribution (*top*) and line profiles (*bottom*) of [Fe II] 1.664/2.047/2.133 μm lines in B5-IRS 1 (left) and HH 34 IRS (right). Those of [Fe II] 1.644 μm are also shown in each plot by grey solid lines. The spatial distribution is measured along the jet, by binning the intensity from -155 to -100 km s^{-1} in B5-IRS 1 and -120 to -60 km s^{-1} in HH 34 IRS. The line profiles are extracted at the driving source, i.e., $-0.2''$ to $0.7''$ at B5-IRS 1 and $-0.3''$ to $0.5''$ at HH 34 IRS.

Table 1. Target information

Object	Distance ^a (pc)	$V_{\text{LSR}}^{\text{b}}$ (km s ⁻¹)	Flow inclination ^c (deg.)	Slit P.A. (deg.)	Orientation	Band	Total on-source integration ^d (s)
SVS 13	300	+8	20–40	159	along the jet	<i>H</i>	1440
				159	along the jet	<i>K</i>	480
				69	perp. to the jet	<i>K</i>	480
B5 IRS1	300	+10	~80	73	along the jet	<i>H</i>	1440
				73	along the jet	<i>K</i>	1200
HH 34 IRS	450	+8.5	23–28	167	along the jet	<i>H</i>	1440
				167	along the jet	<i>K</i>	1200

^aSee text.

^bThe Local Standard of Rest velocity of the parent cloud measured by Knee & Sandel (2000), Yu et al. (1999), and Chernin & Masson (1995).

^cTo the line of sight. See Appendix A for details.

^dIncluding those with the opposite slit angle (i.e., P.A. + 180°).

Table 2: H₂ fluxes normalized to the 1–0 S(1) flux

Object	Region	1–0 S(9)	1–0 S(8)	1–0 S(7)	2–1 S(4)	1–0 S(2)	2–1 S(3)	1–0 S(1)	2–1 S(2)
		1.688 μm	1.715 μm	1.748 μm	2.004 μm	2.034 μm	2.073 μm	2.122 μm	2.154 μm
SVS 13	1	0.02±0.01	0.01±0.01	0.13±0.02	<0.06	0.29±0.01	0.07±0.01	1.00±0.01	0.03±0.01
	2	<0.04	<0.02	0.11±0.09	<0.07	0.23±0.13	<0.13	1.00±0.02	0.05±0.02
	3	0.05±0.01	0.03±0.01	0.12±0.04	<0.04	0.33±0.05	0.08±0.06	1.00±0.01	<0.02
B5-IRS 1	1	<0.01	<0.01	0.15±0.02	<0.04	0.34±0.02	0.10±0.01	1.00±0.01	0.04±0.01
	2	<0.06	<0.09	0.34±0.10	<0.43	0.38±0.10	0.16±0.07	1.00±0.08	0.15±0.07
HH 34 IRS	1	<0.06	<0.06	0.08±0.06	<0.12	0.35±0.03	0.05±0.03	1.00±0.03	0.09±0.03
	3–2 S(3)	1–0 S(0)	2–1 S(1)	3–2 S(2)	3–2 S(1)	1–0 Q(1)	1–0 Q(2)	1–0 Q(3)	1–0 Q(4)
	2.201 μm	2.223 μm	2.248 μm	2.287 μm	2.386 μm	2.407 μm	2.413 μm	2.424 μm	2.437 μm
	<0.02	0.24±0.01	0.08±0.01	<0.01	<0.03	0.89±0.02	0.25±0.02	0.79±0.02	0.25±0.01
	<0.02	0.21±0.02	0.11±0.07	—	—	0.85±0.47	—	0.92±0.35	0.71±0.48
	0.03±0.01	0.22±0.01	0.12±0.03	—	—	0.61±0.22	—	1.22±0.15	0.42±0.04
	<0.02	0.32±0.01	0.11±0.01	<0.02	<0.03	1.12±0.03	0.35±0.02	1.06±0.02	0.31±0.02
	<0.07	0.24±0.05	0.09±0.05	<0.07	<0.12	1.19±0.14	0.08±0.08	0.92±0.12	0.30±0.09
	<0.05	0.27±0.02	0.08±0.02	<0.03	<0.10	1.04±0.06	0.32±0.10	0.88±0.05	0.27±0.04

Table 3: [Fe II] fluxes normalized to the 1.644 μm flux.

Object	Region	A_V	${}^4D_{5/2} \rightarrow {}^4F_{9/2}$ 1.533 μm ($E_u=1.04$ eV) ^a	${}^4D_{3/2} \rightarrow {}^4F_{7/2}$ 1.600 μm (1.08 eV)	${}^4D_{7/2} \rightarrow {}^4F_{9/2}$ 1.644 μm (0.99 eV)	${}^4D_{1/2} \rightarrow {}^4F_{5/2}$ 1.664 μm (1.10 eV)	${}^4D_{3/2} \rightarrow {}^4F_{5/2}$ 1.712 μm (1.08 eV)	${}^4D_{1/2} \rightarrow {}^4F_{3/2}$ 1.745 μm (1.10 eV)	
SVS 13	1	0	0.37±0.02	0.31±0.02	1.00±0.02	0.13±0.01	—	—	
		20	0.54±0.03	0.36±0.02	1.00±0.02	0.12±0.01	—	—	
B5-IRS 1	1	0	0.23±0.03	0.20±0.02	1.00±0.02	0.13±0.02	0.08±0.01	<0.05	
		20	0.34±0.04	0.23±0.02	1.00±0.02	0.12±0.02	0.06±0.01	<0.03	
	2	0	0.17±0.02	0.21±0.02	1.00±0.02	0.15±0.02	0.08±0.02	0.04±0.03	
		20	0.25±0.03	0.25±0.02	1.00±0.02	0.14±0.02	0.07±0.01	0.03±0.02	
	3	0	0.22±0.03	0.23±0.03	1.00±0.03	0.24±0.03	0.10±0.03	0.07±0.04	
		20	0.32±0.05	0.26±0.03	1.00±0.03	0.23±0.03	0.08±0.02	0.05±0.03	
	4+5	0	—	0.13±0.04	1.00±0.05	0.09±0.05	0.06±0.05	<0.06	
		20	—	0.15±0.05	1.00±0.05	0.09±0.05	0.05±0.04	<0.05	
HH 34 IRS	1	0	0.32±0.01	0.20±0.01	1.00±0.01	0.12±0.01	0.09±0.01	0.06±0.01	
		30	0.56±0.02	0.25±0.01	1.00±0.01	0.11±0.01	0.07±0.01	0.04±0.01	
	2	0	0.28±0.01	0.21±0.01	1.00±0.01	0.13±0.01	0.07±0.01	0.07±0.01	
		15	0.37±0.01	0.24±0.01	1.00±0.01	0.13±0.01	0.06±0.01	0.06±0.01	
	3	0	0.21±0.01	0.15±0.01	1.00±0.01	0.10±0.01	0.05±0.01	0.04±0.01	
		15	0.28±0.01	0.17±0.01	1.00±0.01	0.09±0.01	0.04±0.01	0.03±0.01	
	4	0	—	0.11±0.01	1.00±0.01	0.09±0.01	0.04±0.01	0.05±0.01	
		15	—	0.12±0.01	1.00±0.01	0.08±0.01	0.03±0.01	0.04±0.01	
	Object	Region	A_V	${}^4P_{3/2} \rightarrow {}^4D_{7/2}$ 1.749 μm ($E_u=1.70$ eV) ^a	${}^2P_{1/2} \rightarrow {}^4P_{1/2}$ 2.007 μm (2.34 eV)	${}^2P_{3/2} \rightarrow {}^4P_{5/2}$ 2.047 μm (2.28 eV)	${}^4P_{3/2} \rightarrow {}^4D_{1/2}$ 2.072 μm (1.70 eV)	${}^2P_{3/2} \rightarrow {}^4P_{3/2}$ 2.133 μm (2.28 eV)	${}^2P_{3/2} \rightarrow {}^4P_{1/2}$ 2.244 μm (2.28 eV)
	SVS 13	1	0	<0.14	0.40±0.31	<0.23	<0.14	0.11±0.05	<0.11
20			<0.10	0.17±0.13	<0.09	<0.05	0.04±0.02	<0.03	
B5-IRS 1	1	0	<0.02	<0.08	0.026±0.018	<0.03	0.030±0.016	<0.02	
		20	<0.02	<0.03	0.010±0.007	<0.01	0.010±0.005	<0.007	
	2	0	—	<0.08	0.025±0.018	0.041±0.017	0.047±0.017	<0.01	
		20	—	<0.03	0.010±0.007	0.015±0.006	0.016±0.006	<0.004	
	3	0	—	<0.17	<0.02	0.03±0.03	<0.02	<0.06	
		20	—	<0.07	<0.009	0.01±0.01	<0.007	<0.02	
	4+5	0	<0.11	<0.11	<0.06	<0.04	<0.05	<0.04	
		20	<0.08	<0.05	<0.02	<0.02	<0.02	<0.01	
HH 34 IRS	1	0	<0.015	<0.03	0.066±0.005	<0.007	0.028±0.004	0.017±0.003	
		30	<0.009	<0.007	0.016±0.001	<0.002	0.006±0.001	0.003±0.001	
	2	0	<0.005	<0.08	0.058±0.003	<0.005	0.032±0.003	0.015±0.002	
		15	<0.004	<0.04	0.028±0.002	<0.002	0.014±0.001	0.006±0.001	
	3	0	<0.012	<0.03	<0.004	<0.005	0.008±0.004	<0.002	
		15	<0.009	<0.01	<0.002	<0.002	0.004±0.002	<0.001	
	4	0	0.011±0.010	—	<0.005	<0.005	0.010±0.004	<0.005	
		15	0.009±0.008	—	<0.003	<0.002	0.004±0.002	<0.002	

^aUpper energy level from the ground state.

Table 4. Estimated extinction and excitation temperatures of H₂ emission line regions.

Object	Region	A_V			$T_{2-1S(1)/1-0S(1)}$ (10 ³ K)
		S(1)/Q(3)	S(0)/Q(2)	S(2)/Q(4)	
SVS 13	1	6.1±0.8	<1	15±2	1.92±0.06
	2	—	—	—	2.1 ±0.5
	3	28±6	—	30±6	2.1 ±0.2
B5-IRS 1	1	19±1	<6	16±3	2.05±0.06
	2	14±6	—	16±14	1.9 ±0.4
HH 34 IRS	1	12±3	<40	12±6	1.9 ±0.1

Table 5. Estimated extinction in [Fe II] emission line regions.

Object	Region	A_V	
		$I_{1.712}/I_{1.600}$	$I_{1.745}/I_{1.664}$
SVS 13	1	—	—
B5-IRS 1	1	20±10	—
	2	20±10	—
	3	30±20	—
	4+5	<50	—
HH 34 IRS	1	32±6	<8
	2	15±5	<14
	3	15±7	<8
	4	<30	<30